Nano Research Energy

ISSN 2791-0091 CN 10-1944/O6
https://doi.org/10.26599/NRE.2026.9120257

Research Article

Multidentate coordination chemistry remodeling solvation sheath and interfacial evolution for robust aqueous Zn battery

Hongwei Wang[1], Wenyu Xu[1], Binfen Wang[1], Zelin Chang[1], Jialin Li[1], Yunchong Feng[1], Tinghui Xiao[1,2](✉), Hongbo Ding[1](✉), Xinliang Li(✉)

[1] School of Physics and Laboratory of Zhongyuan Light, Zhengzhou University, Zhengzhou 450052, China

[2] Department of Chemistry, School of Science, The University of Tokyo, Tokyo, 113-0033, Japan

Nano Research Energy, **Just Accepted Manuscript** • https://doi.org/10.26599/NRE.2026.9120257

https://www.sciopen.com/journal/2791-0091 on Jul. 29, 2026

Just Accepted

Table of contents

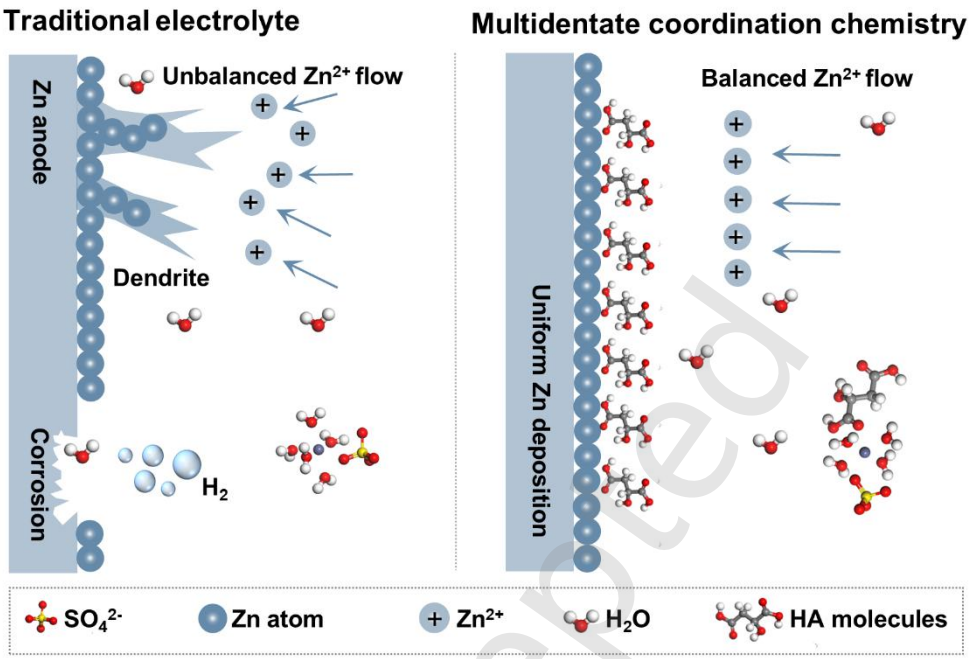

A novel strategy utilizing the multidentate coordination between Zn^{2+} and solvent molecules is presented to concurrently regulate the solvation structure and optimize interfacial mass-charge transfer. Restructuring the intrinsic hydrogen-bond network and interfacial chemistry remarkably inhibits parasitic reactions, guaranteeing homogeneous Zn plating.

ISSN 2791-0091 (print); 2790-8119 (online)
https://doi.org/10.26599/NRE.2026.9120257
Research Article

Multidentate coordination chemistry remodeling solvation sheath and interfacial evolution for robust aqueous Zn battery

Hongwei Wang[1], Wenyu Xu[1], Binfen Wang[1], Zelin Chang[1], Jialin Li[1], Yunchong Feng[1], Tinghui Xiao[1,2] (✉), Hongbo Ding[1] (✉), and Xinliang Li[1] (✉)

[1]School of Physics and Laboratory of Zhongyuan Light, Zhengzhou University, Zhengzhou 450052, China.
[2]Department of Chemistry, School of Science, The University of Tokyo, Tokyo, 113-0033, Japan

Received: 15 June 2026 / **Revised:** 9 July 2026 / **Accepted:** 13 July 2026(已核对)

Abstract

Aqueous Zn-ion batteries represent a promising platform for grid-scale energy storage, yet the advancement is constrained by persistent interfacial challenges on dendrite growth and parasitic corrosion. Herein, a novel strategy leveraging the multidentate coordination of Zn^{2+} and solvent molecules is introduced to synergistically tailor the solvation sheath and modulate the interfacial mass-charge conduction. Reconfiguring the inherent H-bond network and interfacial chemistry effectively suppresses side reactions and ensures uniform Zn deposition. Consequently, a Zn||Zn battery delivers an exceptional cumulative plating capacity of 23.0 $Ah \cdot cm^{-2}$ and operates steadily for over 4600 h under harsh conditions of 10 $mA \cdot cm^{-2}$. When coupled with an I_2 cathode, the full battery retains excellent durability across 65000 cycles at 10 $A \cdot g^{-1}$, with an ultralow capacity decay of 0.0004% per cycle. A practical pouch battery delivers 11.5 mAh and maintains 90.0% capacity after 130 cycles. Multiscale spectroscopy and computations elucidate ligand exchange within the solvation sheath and the synergy with a dynamic interfacial adsorption layer, establishing a green and efficient molecular strategy for stabilizing Zn electrochemistry.

Keywords: aqueous Zn battery, Zn anode, multidentate coordination chemistry, solvation reconfiguration, iodine battery

1 Introduction

The escalating integration of renewable energy sources has intensified the demand for safe and low-cost battery technologies, establishing them as pivotal enablers of the global energy transition. Rechargeable aqueous Zn-ion batteries (ZIBs) have emerged as promising candidates for large-scale energy storage systems, leveraging inherent safety, environmental friendliness, high theoretical capacity (820 $mAh \cdot g^{-1}$), and a low redox potential (–0.76 V *vs.* standard hydrogen electrode) [1–3]. Nevertheless, the

Address correspondence to Hongbo Ding, dinghb@zzu.edu.cn; Xinliang Li, lixinliang@zzu.edu.cn; Tinghui Xiao, xiaoth@zzu.edu.cn

ISSN 2791-0091 (print); 2790-8119 (online)
https://doi.org/10.26599/NRE.2026.9120257
Research Article

reversibility of Zn anodes is compromised by several interfacial challenges, including metal corrosion, hydrogen evolution reaction (HER), dendrite growth, and byproduct formation [4–6]. Such intertwined concerns collectively impair cycling efficiency and operational longevity, thereby presenting fundamental bottlenecks to the commercial implementation of ZIBs.

To mitigate interfacial instability, research efforts have focused on strategies including protective coatings, structural modifications, and electrolyte engineering [7–10]. By enabling molecular and ionic design, electrolyte engineering offers distinct advantages in regulating ion transport, interfacial reactions, and deposition kinetics, thereby allowing multidimensional optimization from thermodynamic to kinetic control [11, 12]. The concerted action of solvation restructuring, electric double layer engineering, and *in-situ* interphase formation dictates favorable deposition kinetics and crystallographic growth, culminating in homogeneous Zn plating and the passivation of H_2O-induced side reactions [13–15]. Current electrolyte design paradigms mainly include high-concentration electrolytes exemplified by water-in-salt systems, cosolvent or diluent formulations incorporating compounds such as dimethyl sulfoxide or N, N-dimethylformamide, and pH-buffering systems utilizing acetate species [16, 17]. Additional representative methodologies encompass deep eutectic solvents based on acetamide or glycerol, alongside functional additive strategies that introduce compounds like glucose or polyethylene glycol [18–21].

The precise modulation of both the bulk electrolyte structure and electrode-electrolyte interfacial chemistry is paramount for achieving stable Zn electrochemistry. Despite marked improvements, contemporary electrolyte designs still face multiple obstacles, including the high expense from concentrated salts or custom additives, degradation of key properties such as heightened viscosity and lowered ionic conductivity, challenges in production scaling, and potential environmental impacts [22–24]. Consequently, electrolyte design must concurrently enhance electrochemical stability and reversibility without undermining the innate advantages of aqueous electrolytes. Furthermore, practical integration demands compliance with green chemistry guidelines and adherence to the strict economic and environmental standards of grid-scale energy storage [25, 26]. Among available options, small-molecule organic acids offer distinctive benefits for Zn anode regulation, stemming from their high solubility, specific interfacial adsorption, and favorable kinetic tuning [27, 28]. Precise coordination chemistry is expected to provide a viable pathway to achieve efficient solvation restructuring and robust interfacial control, thereby addressing the long-standing issue of electrochemical instability.

Herein, a tailored multidentate coordination strategy is presented to substantially enhance Zn anode electrochemical stability. Capitalizing on the 2-Hydroxybutanedioic acid (HA) molecular framework, the coordinated approach establishes robust multidentate bonding with Zn^{2+}, thereby displacing coordinated H_2O and reconstituting the H-bond network. The coordination further promotes a dynamic molecular barrier through pronounced zincophilicity and interfacial adsorption, concurrently passivating the electrode surface and guiding uniform ion

ISSN 2791-0091 (print); 2790-8119 (online)
https://doi.org/10.26599/NRE.2026.9120257
Research Article

flux. The synergy between solvation restructuring and interfacial modulation yields remarkable cycling reversibility, achieving an exceptional cumulative plating capacity of 23.0 $Ah \cdot cm^{-2}$ and sustaining stable operation for over 4600 h at 10 $mA \cdot cm^{-2}$. Moreover, $Zn||I_2$ batteries demonstrate outstanding durability, maintaining stable operation for 65000 cycles at 10 $A \cdot g^{-1}$ with an ultralow capacity decay rate of 0.0004% per cycle. Multiscale spectroscopic analysis and theoretical modeling collectively elucidate the underlying mechanism, highlighting the cooperative regulation of solvation structure and interfacial chemistry.

2 Results and discussion

2.1 Regulation of the solvation sheath

Unlike conventional monodentate ligands, the biomass-derived HA leverages its dual carboxyl groups to (-COO^-) establish a highly compatible multidentate coordination geometry with Zn^{2+}. Such unique architecture synergistically minimizes steric repulsion and amplifies orbital interactions, driving the aggressive expulsion of H_2O and SO_4^{2-} from the primary solvation shell and significantly lowering the desolvation energy barrier [29]. Molecular dynamics (MD) simulations were employed to elucidate the solvation structure of Zn^{2+}. In the bare $ZnSO_4$ electrolyte (denoted BZS), the dominant configuration is a $Zn^{2+}(H_2O)_{4.9}(SO_4^{2-})_{1.2}$ structure (**Fig. S1 in the Electronic Supplementary Material (ESM)**). The strong polarization of Zn^{2+} renders coordinated H_2O molecules in the inner shell highly reactive. Introducing trace HA into the $ZnSO_4$ electrolyte (denoted HZS) leads to its incorporation into the solvation environment, partially replacing first-shell H_2O and SO_4^{2-} (**Fig. 1(a)**). Analyses of the radial distribution function (RDF) and coordination number analyses quantitatively confirm this structural restructuring. Driven by competitive coordination, the average hydration number decreases from 4.9 to 4.7, accompanied by a reduction in SO_4^{2-} coordination from 1.2 to 1.1 (**Fig. 1(b)**). The resulting solvation complex can be described as $Zn^{2+}(H_2O)_{4.7}(SO_4^{2-})_{1.1}HA_{0.03}$. By reducing the population of activated H_2O molecules in the primary shell, this tailored coordination environment effectively suppresses parasitic reactions at the Zn anode interface.

Energy decomposition analysis (EDA) was employed to quantify the fundamental interactions governing Zn^{2+} coordination, decomposing the total interaction energy into electrostatics (E_{els}), exchange-repulsion (E_{xrep}), orbital interactions (E_{orb}), and dispersion forces (E_{disp}) [27, 30]. As presented in **Fig. 1(c)**, a comparative assessment of Zn^{2+}-HA versus Zn^{2+}-H_2O coordination reveals strikingly divergent energy profiles. The Zn^{2+}-HA exhibits significantly more favorable E_{els} (–16.24 eV) relative to the Zn^{2+}-H_2O (–10.79 eV), directly confirming the superior charge anchoring capability conferred by the dicarboxyl groups. Concurrently, the Zn^{2+}-HA displays a lower E_{xrep} (4.30 *vs.* 3.17 eV) and an enhanced E_{orb} (–7.75 *vs.* –8.20 eV) compared to Zn^{2+}-H_2O. Such an energetic distribution signifies diminished steric repulsion and increased covalent character within the Zn^{2+}-HA, collectively underscoring the advantages of the multidentate mode in terms of geometric compatibility and electronic binding. Moreover, the E_{disp} suggests that competitive displacement of water molecules by HA does not incur a substantial energy penalty

ISSN 2791-0091 (print); 2790-8119 (online)
https://doi.org/10.26599/NRE.2026.9120257
Research Article

regarding dispersion forces.

The electrostatic properties of the ligands were investigated through electrostatic potential (ESP) analysis. As illustrated in **Fig. 1(d)**, regions of negative potential are predominantly localized on O atoms. Notably, the carboxylate O exhibits a significantly more negative electrostatic potential (–9.86 eV) than that of H_2O (–1.80 eV). The marked electrostatic contrast promotes preferential chelation between $-COO^-$ and Zn^{2+}, driving the formation of a stable multidentate coordination structure. Binding energy calculations further support this coordination preference. The substantially more negative Zn^{2+}-HA binding energy (–27.77 eV) compared to that of Zn^{2+}-H_2O (–4.39 eV) provides the thermodynamic driving force for the spontaneous displacement of coordinated H_2O (**Fig. 1(e)**).

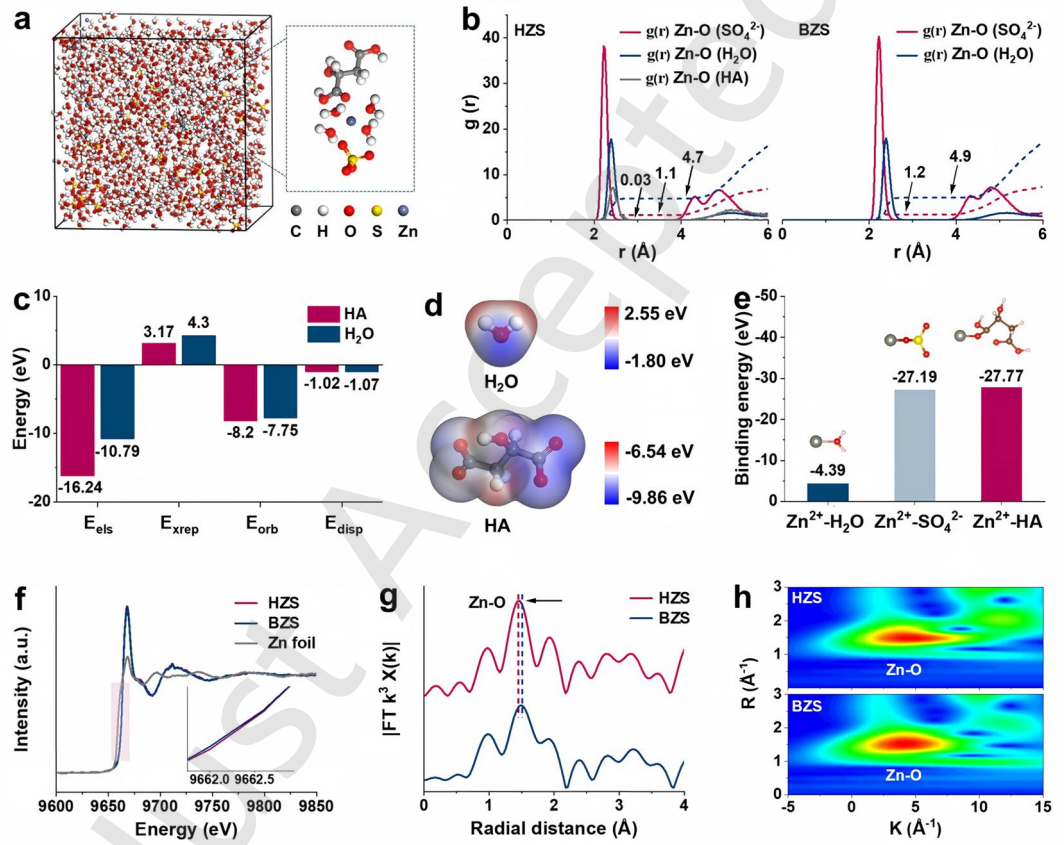

Figure 1 Regulation of the solvation sheath. (a) 3D snapshot from MD simulations of HZS electrolyte. Inset: magnified view of Zn^{2+} solvation structure within dashed-line box. (b) RDFs and coordination number of Zn^{2+} collected from MD simulations. (c) EDA results of Zn^{2+} solvation sheath constituents. (d) ESP mapping of H_2O and HA. (e) The binding energies of H_2O, SO_4^{2-}, and HA with Zn^{2+}. (f) Zn K-edge XANES spectra. The inset is the enlarged expanded view of the purple-marked region. (g) K^3-weighted FT-EXAFS spectra. (h) Wavelet transform contour plots of Zn K-edge in *R*-space.

X-ray absorption fine structure (XAFS) spectroscopy was employed to directly probe the electronic states and local coordination structure of Zn^{2+}. As shown in **Fig. 1(f)**, the Zn K-edge X-ray absorption near-edge structure (XANES) spectrum displays

ISSN 2791-0091 (print); 2790-8119 (online)
https://doi.org/10.26599/NRE.2026.9120257
Research Article

a shift toward higher energy in the HZS electrolyte, suggesting a modulated electronic density around the Zn^{2+} centers. Furthermore, Fourier-transform extended X-ray absorption fine structure (FT-EXAFS) spectra further exhibit a shortened Zn-O bond length in the HZS electrolyte, attributed to the substitution of water by strongly coordinating HA ligands in the primary solvation shell (**Fig. 1(g)**). Wavelet-transform EXAFS was employed to gain deeper insight into the coordination configuration (**Fig. 1(h)**). The resulting profiles reveal a narrowed Zn-O peak distribution in *R*-space, accompanied by extended *K*-space features and enhanced backscattering amplitude in high-*K* regions. Bidirectional configuration changes characterized by *R*-space contraction and *K*-space extension denote spatial constraints imposed by multidentate coordination, which effectively limit the conformational freedom of the solvation structure.

Density functional theory (DFT) calculations were performed to quantitatively probe the molecular adsorption energetics behavior on the Zn anode (**Fig. S2 in the ESM**). HA demonstrates a significantly stronger adsorption energy (–7.55 eV) than H_2O (–1.26 eV), representing an approximate sixfold enhancement. The prominent zincophilic character drives the *in situ* assembly of a dense molecular overlayer serving as a physical barrier, which effectively suppresses both HER and corrosion reactions. Electrolyte wettability was further characterized through contact angle measurements (**Fig. S3 in the ESM**). The contact angle of the HZS electrolyte on the Zn anode is 89.8°, significantly lower than the 102.7° value measured for the BZS electrolyte. Such improved wettability enhances electrolyte-electrode contact, facilitates more efficient ion diffusion, and homogenizes the Zn^{2+} flux during deposition [31].

2.2 From solvation regulation to stabilized interfacial chemistry

Multiscale spectroscopic characterization elucidates a cascade of structural transformations within the solvation structure, initiated by multidentate coordination. As illustrated in **Fig. 2(a)**, a slight upfield shift from 4.743 to 4.737 ppm is detected in H_2O proton signals *via* proton nuclear magnetic resonance (^{1}H NMR). The shift toward a higher field reflects an increase in local electron density and an enhanced shielding effect, indicative of a weakened H-bond network among H_2O molecules [32]. Raman spectroscopy further tracks the evolution of H-bond strength and Zn^{2+} solvation environment. Spectral deconvolution shows decreased proportions of both weak and strong H-bonds in the HZS electrolyte, whereas medium-strength H-bonds increase from 46.6% to 50.8% (**Fig. 2(b)** and **Fig. S4 in the ESM**). The redistribution drives the reorganization of the aqueous environment into a more stable and ordered H-bond framework. Furthermore, the vibrational mode of SO_4^{2-} (v-SO_4^{2-}) indicates a reconfiguration of ion pairing structures in the HZS electrolyte (**Fig. 2(c)**). The proportion of contact ion pairs (CIP) decreases from 9.3% to 7.1%, while that of solvent-separated ion pairs (SSIP) increases correspondingly, attributed to the modulation of the solvation shell by the newly formed Zn^{2+}-HA species.

In situ Raman spectroscopy was utilized to dynamically monitor the electrochemical evolution at the electrode-electrolyte interface. Variations in Zn^{2+}

ISSN 2791-0091 (print); 2790-8119 (online)
https://doi.org/10.26599/NRE.2026.9120257
Research Article

concentration were tracked by analyzing the spectral signatures of SO_4^{2-} (**Fig. 2(d)**). The HZS electrolyte maintained consistent SO_4^{2-} intensity during deposition, which reflects the Znophilic-group-induced anion-rich interphase coordinating ion transport with Zn^{2+} electroreduction kinetics, thereby mitigating interfacial concentration polarization. In contrast, the SO_4^{2-} peak intensity in the BZS electrolyte progressively decreased during Zn deposition, consistent with the formation of an anion depletion layer. The behavior arises from the anion migration away from the interface, driven by localized Zn^{2+} depletion near the electrode surface [33]. Spectral changes in O-H stretching vibrations further reflected dynamic H_2O behavior at the interface (**Fig. 2(e)**). The Zn anode in the HZS electrolyte exhibited gradually attenuated O-H signals during repeated plating/stripping cycles, confirming the effective displacement of interfacial H_2O by the anion-rich layer and consequent suppression of parasitic reactions. Conversely, the Zn anode in the BZS electrolyte showed persistently intense O-H peaks, signifying sustained high activity of interfacial H_2O throughout cycling.

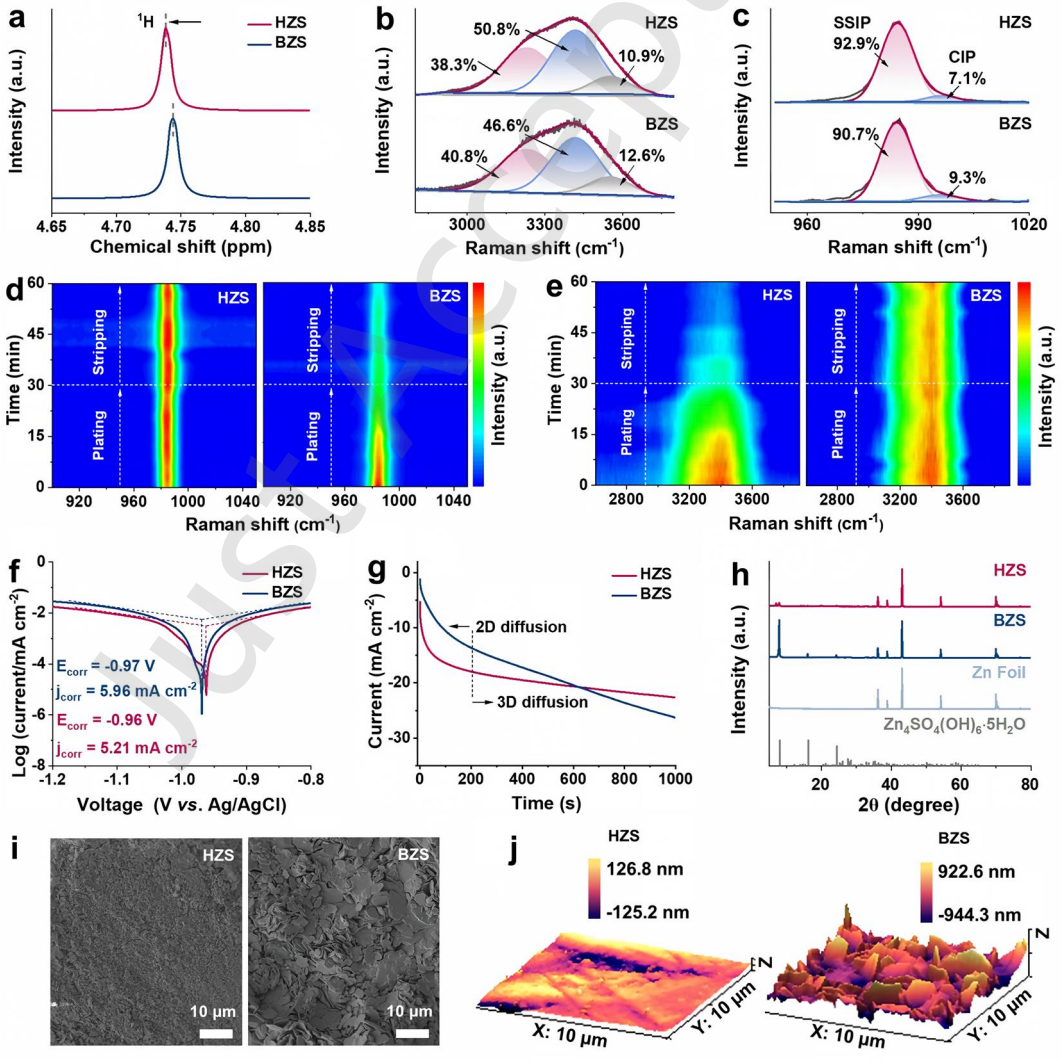

Figure 2 From solvation regulation to stabilized interfacial chemistry. (a) ^1H NMR spectra. (b) The fitted Raman spectra of O-H stretching and proportions of different H-bonds. (c) The fitted Raman spectra of the v-SO_4^{2-} and the proportions of CIP and

ISSN 2791-0091 (print); 2790-8119 (online)
https://doi.org/10.26599/NRE.2026.9120257
Research Article

SSIP. (d) *In situ* Raman spectra of v-SO_4^{2-} during the plating/stripping process. (e) The O-H stretching vibration during the plating/stripping process. (f) Tafel curves in HZS and BZS electrolyte. (g) Chronoamperometry curves of Zn||Zn batteries at a constant potential of –150 mV. (h) XRD patterns of Zn anodes after 50 cycles at 10 mA·cm^{-2}/1 mAh·cm^{-2}. (i) SEM images of cycled Zn anodes (50 cycles, 10 mA·cm^{-2}/1 mAh·cm^{-2}) in HZS and BZS electrolyte. (j) AFM topographic maps of Zn anodes post-cycling (50 cycles, 10 mA·cm^{-2}/1 mAh·cm^{-2}) in HZS and BZS electrolyte.

High-resolution X-ray photoelectron spectroscopy (XPS) further corroborates the stable interfacial molecular adsorption and the shielding effect (**Fig. 5 in the ESM**). After 10 cycles in the HZS electrolyte, the C 1s spectrum of the Zn anode exhibits an enhanced peak at 288.6 eV (from 7.7% to 8.0%), assigned to chemisorbed -COO^- groups. Concurrently, the pronounced attenuation of both the O 1s peak at ~532.2 eV associated with O-H bonds and the S 2p peak at 168.3 eV derived from SO_4^{2-} anions further verifies the formation of a dense molecular overlayer. The robust barrier effectively isolates the electrode from free H_2O and SO_4^{2-} anions, thereby shutting down parasitic decomposition pathways. Electrochemical characterization further evaluated the stability of the constructed anion-rich interfacial layer. As depicted in **Fig. 2(f)**, the introduction of HA induces a positive shift in the corrosion potential from –0.97 to –0.96 V, concomitant with a reduction in the corrosion current density from 5.96 to 5.21 mA·cm^{-2}, demonstrating enhanced stability and corrosion resistance [34]. Additionally, the kinetic suppression of HER is evidenced by linear sweep voltammetry (**Fig. 6 in the ESM**). The HZS electrolyte increases the overpotential by 13 mV at 10 mA·cm^{-2}, an effect ascribed to the molecular adsorption layer that hinders proton reduction kinetics.

To elucidate the transition in nucleation and deposition behavior, chronoamperometry curves were recorded for Zn||Zn batteries (**Fig. 2(g)**). In the BZS electrolyte, the current density continuously increases with time, characteristic of a prolonged 2D diffusion process that favors uncontrolled dendritic propagation. In contrast, the battery utilizing the HZS electrolyte exhibits rapid nucleation within the initial 200 s, after which the current density stabilizes, consistent with a self-limiting, diffusion-controlled 3D growth model (**Fig. 7 in the ESM**) [35]. Electrochemical impedance spectroscopy performed on Zn||Zn batteries further illuminates the ion transport characteristics (**Fig. S8 in the ESM**). The Nyquist plot reveals a prominent 64% reduction in the overall impedance for the HZS electrolyte (175 to 63 Ω) relative to the BZS electrolyte, demonstrating enhanced ionic conduction and interfacial kinetics.

Interfacial composition and morphological analysis were performed to satisfy the validation of electrode-electrolyte chemistry regulation. As presented in **Fig. 2(h)**, the Zn anode cycled in the HZS electrolyte displays no detectable diffraction peaks associated with crystalline byproducts. In marked contrast, the anode cycled in the BZS electrolyte exhibits sharp diffraction peaks characteristic of $Zn_4SO_4(OH)_6{\cdot}xH_2O$ (8.0°, 16.2°, and 24.4°). These crystallographic contrasts confirm the high efficacy of

ISSN 2791-0091 (print); 2790-8119 (online)
https://doi.org/10.26599/NRE.2026.9120257
Research Article

the dense molecular overlayer in suppressing the nucleation and growth of passivating byproducts. Scanning electron microscopy (SEM) images of cycled Zn anodes provide direct morphological evidence of interfacial regulation. As depicted in **Fig. 2(i)** and **Fig. S9 in the ESM**, unlike the randomly oriented, coarse dendrites observed in the BZS system, the deposition topography in the HZS electrolyte features a compact and uniformly nanocrystalline architecture, accompanied by a noticeable reduction in average grain size. The manifest transition from a disordered microscale to an ordered nanoscale regime demonstrates the effective control over Zn nucleation and growth imposed by the adsorbed molecular interphase. Additionally, atomic force microscopy (AFM) was employed to quantify the surface morphology (**Fig. 2(j)** and **Fig. S10 in the ESM**). A peak-to-valley height difference of 1866.9 nm, characteristic of three-dimensional island growth, was measured for the Zn anode deposited in the BZS electrolyte. In contrast, the Zn anode cycled in the HZS electrolyte exhibits exceptional planarity, with height variation reduced to 252.0 nm. The dramatic smoothing corroborates that the tailored interfacial chemistry steers deposition away from an unstable island-growth mode toward a stable, quasi-two-dimensional mechanism.

2.3 Probing Zn nucleation and deposition *via* XAFS

XAFS spectroscopy was employed to probe the evolution of the local coordination geometry and electronic states of the Zn anode. As depicted in **Fig. 3(a)**, the Zn K-edge XANES spectra of the anode cycled in the HZS electrolyte demonstrate exceptional stability throughout cycling and align closely with the spectral signature of the bare Zn, indicating the formation of a stable and reversible interfacial state. Conversely, the Zn anode cycled 200 times in the BZS electrolyte displays a significant attenuation of the white line peak intensity, accompanied by the emergence of additional absorption features at other energy positions. Such spectral alterations reflect a decreased average oxidation state of the interfacial Zn species and the formation of electrochemically inactive metallic Zn [36]. A magnified view of the K-edge further elucidates the chemical state evolution during cycling. As shown in **Fig. 3(b)**, the K-edge for the Zn anode cycled in the HZS electrolyte remains notably stable. In contrast, cycling in the BZS electrolyte results in a discernible low-energy shift of the K-edge after 200 cycles. Collectively, these observations demonstrate that the interfacial regulation mediated by the molecular adsorption layer effectively suppresses the accumulation of electrochemically inert “dead Zn”, thereby preserving a stable and reversible interfacial chemistry throughout extended cycling.

FT-EXAFS analysis was performed to elucidate the evolution of microstructural order within the Zn deposits. As shown in **Fig. 3(c)** and **Fig. S11 in the ESM**, the Zn anode cycled in the BZS electrolyte suffers an approximately 50% decay in Zn-Zn coordination peak intensity after 200 cycles, accompanied by a pronounced enhancement of the Zn-O coordination signal. The stark contrast underscores the highly irreversible nature of Zn plating and stripping, which disrupts local metallic ordering and drives the transformation into a disordered, oxygen-rich compound state. Conversely, the Zn anode cycled in the HZS electrolyte reveals a distinctly different

ISSN 2791-0091 (print); 2790-8119 (online)
https://doi.org/10.26599/NRE.2026.9120257
Research Article

structural evolution. Throughout cycling, the Zn-Zn coordination peak exhibits only a minor positional shift (2.30 to 2.35 Å) alongside stable intensity with negligible decay, collectively attesting to the formation of a structurally robust Zn deposit.

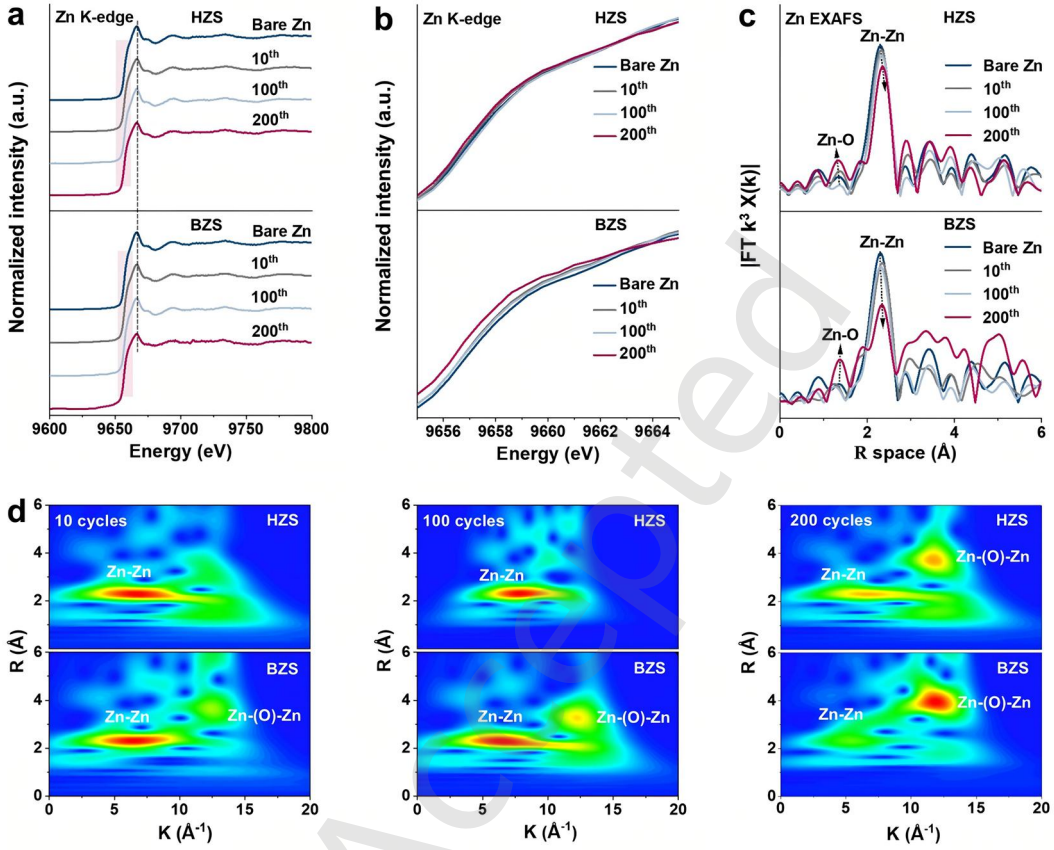

Figure 3 Probing Zn nucleation and deposition *via* XAFS. (a) Zn K-edge XANES spectra of bare Zn and cycled anodes (10, 100, 200 cycles) in HZS and BZS electrolyte. (b) Expanded view of absorption edge regions. (c) K^3-weighted FT-EXAFS spectra of bare Zn and cycled anodes (10, 100, 200 cycles). (d) Wavelet transform contour plots of Zn *K*-edge after 10, 100, and 200 cycles of Zn anodes.

Wavelet-transform EXAFS contour mapping further visualizes the local structural evolution (**Fig. 3(d)** and **Fig. S12 in the ESM**). In the HZS electrolyte, the Zn-Zn peak corresponding to the first coordination shell of metallic Zn remains stable throughout cycling. After 200 cycles, only a weak new scattering peak emerges near 3.7 Å, attributed to the originating from an O-bridged Zn-Zn [Zn-(O)-Zn] scattering path, which suggests trace formation of crystalline by-products such as basic Zn sulfate. The low intensity of this feature indicates effective suppression of such side reactions. Conversely, the BZS electrolyte exhibits a marked increase in signal intensity within the 3.6–4.0 Å range upon cycling, corresponding to the substantial generation and accumulation of insulating by-products (e.g., $Zn_4SO_4(OH)_6{\cdot}xH_2O$). Concurrently, the primary Zn-Zn peak intensity around 2.3 Å diminishes significantly. Collectively, the reconstruction of the interfacial chemical environment by the molecular adsorption layer redirects the deposition mechanism away from a detrimental pathway associated with disordered “dead Zn” and extensive by-product

ISSN 2791-0091 (print); 2790-8119 (online)
https://doi.org/10.26599/NRE.2026.9120257
Research Article

formation, promoting a stable and highly reversible metallic deposition regime.

2.4 Enhanced electrochemical performances

The nucleation kinetics of Zn^{2+} were investigated *via* cyclic voltammetry (CV) using Zn||Cu batteries. As illustrated in **Fig. 4(a)**, the HZS electrolyte reduces the nucleation overpotential (NOP) by 17.9 mV, signifying lowered nucleation barriers and accelerated deposition kinetics. Further evaluation under a high current density (20 $mA \cdot cm^{-2}$/1 $mAh \cdot cm^{-2}$) shows that the Zn||Cu batteries employing the HZS electrolyte achieve an initial NOP of 80 mV, representing a reduction of over 40% compared to the BZS electrolyte (140 mV). The evident decrease demonstrates enhanced interfacial charge-transfer kinetics (**Fig. 4(b)**). Furthermore, throughout cycling, the batteries with the HZS electrolyte exhibit consistently smaller and more stable voltage hysteresis (498 mV) compared to the BZS counterpart (789 mV), underscoring a substantial improvement in reversibility (**Fig. 4(c)** and **Fig. S13 in the ESM**).

Long-term cycling stability and Coulombic efficiency (CE) of Zn||Cu batteries are key indicators of Zn reversibility (**Fig. 4(d)**). Notably, the Zn||Cu batteries with the HZS electrolyte achieve an extended lifespan of 1200 cycles at 20 $mA \cdot cm^{-2}$/1 $mAh \cdot cm^{-2}$, while maintaining an average CE of 99.5%. In contrast, the Zn||Cu batteries with BZS electrolyte suffer a rapid decay in efficiency after just 400 cycles under the same conditions. The universal applicability of the HZS electrolyte across different deposition substrates was further evaluated using Zn||Ti batteries (**Fig. S14 in the ESM**). Utilizing the HZS electrolyte, the Zn||Ti batteries sustain stable cycling over 1600 cycles at 10 $mA \cdot cm^{-2}$/1 $mAh \cdot cm^{-2}$ with highly consistent CE, whereas the BZS system exhibits pronounced CE fluctuations and undergoes premature failure after 1100 cycles. Subsequently, *in situ* EIS was performed during the initial deposition cycles to intuitively track the dynamic interfacial kinetics (**Fig. S15 in the ESM**). In the BZS electrolyte, the charge-transfer resistance (R_{ct}) exhibits a relatively low value and continuously decreases, which is a typical consequence of unconstrained 3D dendritic growth that severely roughens the electrode surface and persistently expands the electrochemically active surface area. Conversely, the R_{ct} value in the HZS electrolyte rapidly stabilizes after the first cycle, verifying the formation of a structurally robust molecular adsorption layer.

The cycling stability was systematically evaluated using Zn||Zn batteries. An initial screening was conducted to identify the optimal HA concentration through a comparative analysis of batteries containing varying additive amounts (**Fig. S16 in the ESM**). Under 1 $mA \cdot cm^{-2}$/1 $mAh \cdot cm^{-2}$, both 0.05 M and 0.2 M HZS electrolytes exhibited slightly shorter service lives than the 0.1 M HZS electrolyte, which delivered a lifespan of 2150 h, thereby confirming 0.1 M as the optimal concentration. To further examine electrode robustness under rigorous operating conditions, subsequent evaluations were performed at elevated current densities. Notably, the Zn||Zn batteries utilizing the HZS electrolyte achieved a cycle lifespan of 4600 h under 10 $mA \cdot cm^{-2}$/1 $mAh \cdot cm^{-2}$ (**Fig. 4(e)**). Under a fixed areal capacity of 1 $mAh \cdot cm^{-2}$ and elevated current densities of 20 and 60 $mA \cdot cm^{-2}$, Zn||Zn batteries with the HZS electrolyte maintained exceptional operational stability, sustaining

ISSN 2791-0091 (print); 2790-8119 (online)
https://doi.org/10.26599/NRE.2026.9120257
Research Article

continuous cycling for over 2150 and 110 h, respectively (**Fig. S17 in the ESM**). The cycling lifetimes correspond to 32-fold and 2.5-fold improvements over the control batteries, demonstrating markedly enhanced durability under extreme conditions. Further validation under high areal capacity conditions confirmed the practical viability of the approach. Under demanding parameters of 10 mA·cm^{-2}/5 mAh·cm^{-2}, Zn||Zn batteries with HZS electrolyte exhibited highly stable voltage profiles and achieved an extended service life of 1000 h (**Fig. 4(f)**). In stark contrast, the BZS control group displayed substantial voltage polarization with distinct fluctuations, failing after approximately 300 h due to short-circuiting. Moreover, at an areal capacity of 10 mAh·cm^{-2}, the cycling lifespan was extended by 2.2-fold (280 h), validating the stability of the reconfigured interfacial chemistry under stringent deposition conditions (**Fig. S18 in the ESM**).

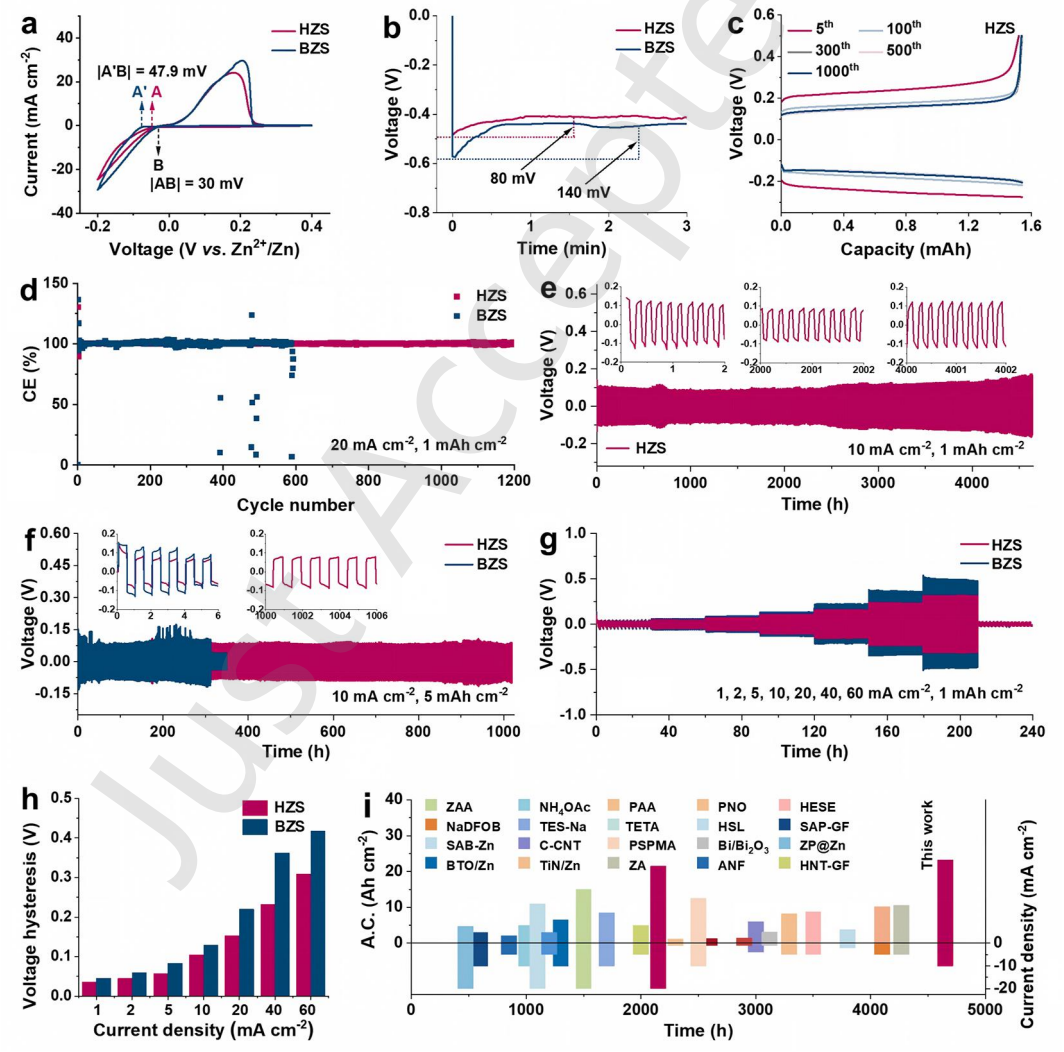

Figure 4 Enhanced electrochemical performances. (a) CV curves of Zn||Cu batteries. (b) NOP of Zn||Cu batteries under 20 mA·cm^{-2}. (c) The corresponding GCD curves at 20 mA·cm^{-2}/1 mAh·cm^{-2} across different cycles. (d) The CE of Zn||Cu batteries at 20 mA·cm^{-2}/1 mAh·cm^{-2}. (e) Cycling performance of Zn||Zn batteries at 10 mA·cm^{-2}/1 mAh·cm^{-2}. (f) Cycling performance of Zn||Zn batteries at 10 mA·cm^{-2}/5 mAh·cm^{-2}. (g) Rate performance of Zn||Zn batteries. (h) Voltage hysteresis during

ISSN 2791-0091 (print); 2790-8119 (online)
https://doi.org/10.26599/NRE.2026.9120257
Research Article

plating/stripping at varied current densities. (i) Comparison of cumulative capacity, cycle life, and current density with other advanced Zn-based battery systems.

Rate performance tests were conducted to further elucidate the improved kinetics. As depicted in Fig. 4(g), the Zn||Zn battery with the HZS electrolyte exhibits significantly reduced voltage polarization and superior voltage stability across current densities ranging from 1 to 60 mA·cm^{-2}. Further insight is provided in Fig. 4(h), which highlights the increasingly pronounced kinetic superiority of the HZS electrolyte under elevated current densities, as evidenced by a voltage hysteresis reduction exceeding 0.1 V. More encouragingly, a comparative analysis with representative studies in terms of current density, cycle life, and cumulative areal capacity demonstrates the remarkable performance of the present system, which achieves unprecedented cumulative capacities of 23.0 and 21.5 Ah·cm^{-2} at 10 and 20 mA·cm^{-2}, respectively. The values significantly exceed those of most contemporary Zn-based battery systems reported to date (**Fig. 4(i)** and **Table S1 in the ESM**) [7, 33, 37–44].

2.5 Practicality verification based on I_2 battery

Zn||I_2 full batteries were assembled to evaluate the practical applicability of the multidentate coordination chemistry strategy. CV reveals that batteries employing the HZS electrolyte exhibit an enhanced current response and a reduced voltage gap between the oxidation and reduction peaks (0.31 to 0.27 V), indicating significantly alleviated polarization and improved electrochemical reversibility (**Fig. 5(a)**). Rate performance was evaluated over current densities from 0.5 to 10.0 mA·cm^{-2}. As shown in **Fig. 5(b)**, the Zn||I_2 batteries with the HZS electrolyte deliver an areal capacity of 1.47 mAh·cm^{-2} at 0.5 mA·cm^{-2} and retain 1.16 mAh·cm^{-2} at 10.0 mA·cm^{-2}, demonstrating exceptional rate capability. Superior areal capacities are maintained at all tested current densities, attributed to facilitated Zn^{2+} desolvation and enhanced ion-transport efficiency. The corresponding galvanostatic charge-discharge (GCD) profiles further corroborate the outstanding rate capability (**Fig. 5(c)** and **Fig. S19 in the ESM**). Throughout current densities ranging from 0.5 to 10 mA·cm^{-2}, batteries with HZS electrolyte exhibit a consistently narrow voltage plateau hysteresis of merely 30 mV, while maintaining well-defined charge/discharge plateaus.

Long-term cycling evaluation confirms the exceptional electrochemical stability enabled by the reconfigured solvation structure and interfacial chemistry. With HZS electrolyte, the Zn||I_2 battery achieves an initial discharge capacity of 157.5 mAh·g^{-1} at 10 A·g^{-1} and maintains 112.2 mAh·g^{-1} after 65,000 cycles (**Fig. 5(d)**). The performance corresponds to an ultralow capacity decay rate of 0.0004% per cycle and an average CE of 99.9%. When the I_2 loading is elevated to 10 mg·cm^{-2}, the Zn||I_2 batteries with the HZS electrolyte provide an initial areal capacity of 1.64 mAh·cm^{-2} at 1 mA·cm^{-2} and sustain 1.23 mAh·cm^{-2} after 700 cycles with a CE of 98.5% (**Fig. 5(e)**). Furthermore, self-discharge evaluations show that the fully charged Zn||I_2 battery retains 87.6% of its capacity after a 24-hour resting period (**Fig. S20 in the ESM**). Practical viability was further demonstrated using pouch batteries with

ISSN 2791-0091 (print); 2790-8119 (online)
https://doi.org/10.26599/NRE.2026.9120257
Research Article

high-mass-loading I_2 electrodes (8.5 mg·cm^{-2}) further demonstrates practical viability. The Zn||I_2 pouch batteries with the HZS electrolyte delivered a total capacity of 11.5 mAh with 90.0% retained capacity after 130 cycles at 5 mA·cm^{-2}, coupled with a CE of 99.0% (**Fig. 5(f)**). Notably, a systematic comparison of Zn||I_2 batteries developed under various optimization strategies was conducted, evaluating cycle number, specific capacity, and current density (**Fig. 5(g)** and **Table S2 in the ESM**). The Zn||I_2 battery developed in this work, based on coordinated solvation and interfacial modulation, demonstrates comprehensive superiority in cycling longevity, rate capability, and specific capacity. Consequently, it outperforms previously reported systems relying solely on electrolyte engineering, structural design, or cathode material optimization [45–50].

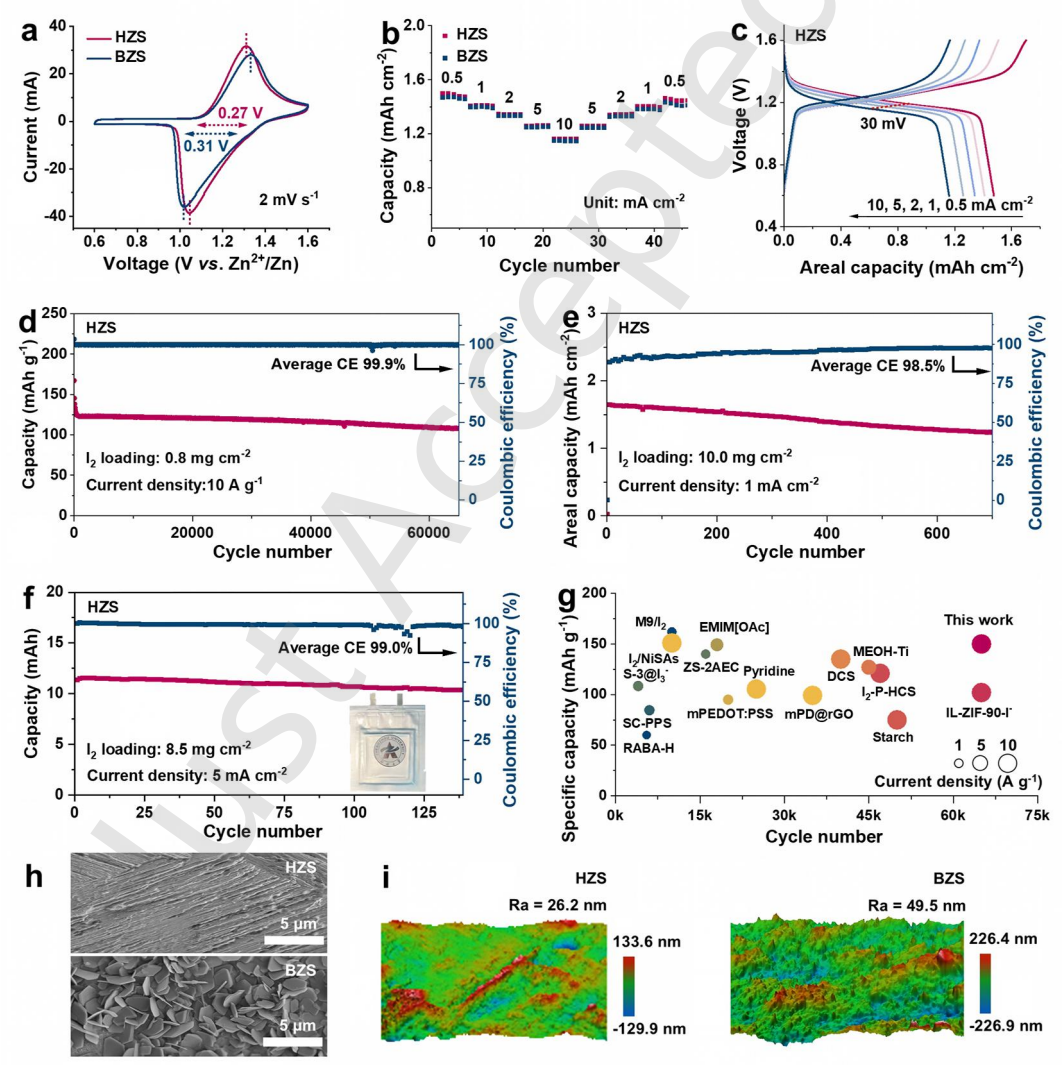

Figure 5 Practicality verification based on I_2 battery. (a) CV curves of Zn||I_2 batteries at 2 mV·s^{-1}. (b) Rate performance of Zn||I_2 batteries from 0.5 to 10 mA·cm^{-2}; the mass loadings of I_2 are about 8.0 mg·cm^{-2}. (c) GCD profiles under various current rates with HZS electrolyte. (d) Long-term cycling of Zn||I_2 batteries at 10 A·g^{-1} with HZS electrolyte; the mass loadings of I_2 are about 0.8 mg·cm^{-2}. (e) Long-term cycling of Zn||I_2 batteries at 1 mA·cm^{-2} with HZS electrolyte; the mass loadings of I_2 are about 10.0 mg·cm^{-2}. (f) Pouch batteries perform at 5 mA·cm^{-2} (I_2 loading: 8.5

ISSN 2791-0091 (print); 2790-8119 (online)
https://doi.org/10.26599/NRE.2026.9120257
Research Article

mg·cm^{-2}) with HZS electrolyte. (g) Comparative benchmarking against state-of-the-art Zn||I_2 batteries. (h) SEM images of Zn anodes after 500 cycles at 5 A·g^{-1}. (i) AFM images of Zn anodes after 500 cycles at 5 A·g^{-1}.

Post-cycling structural characterization of Zn anodes after 500 cycles in Zn||I_2 batteries further validates the efficacy of the HZS electrolyte in regulating deposition behavior within a practical device context. SEM images reveal vertically aligned quasi-hexagonal platelet structures on the anode cycled in the BZS electrolyte (Fig. 5(h)). Under identical cycling conditions, the HZS electrolyte yields flat and compact Zn deposits. The distinct morphological control underscores the capability of the reconfigured interfacial chemistry to inhibit dendritic growth and direct uniform Zn^{2+} deposition. AFM was employed to quantify the surface topography and height variation of cycled Zn anodes (**Fig. 5(i)** and **Fig. S21 in the ESM**). The Zn anode cycled in the BZS electrolyte exhibits an arithmetic mean roughness (R_a) of 49.5 nm, whereas the anode in the HZS electrolyte displays a significantly reduced Ra of 26.2 nm. The resulting smoother electrode morphology substantially lowers the risk of dendrite-induced separator penetration and internal short circuits.

3 Conclusion

In summary, this work presents a molecular multidentate coordination strategy that effectively reconstructs the ion solvation environment and interfacial chemistry in aqueous Zn batteries. Through multidentate coordination, the designed molecular structure forms stable complexes with Zn^{2+}, displacing coordinated H_2O molecules, disrupting the intrinsic H-bond networks, and establishing a dynamically protective interphase. The synergistic regulation enables unprecedented electrochemical stability, delivering a remarkable cumulative plating capacity of 23.0 Ah·cm^{-2} and ultrastable cycling performance extending beyond 4600 h at 10 mA·cm^{-2}. When integrated with an I_2 cathode, the full battery demonstrates outstanding cycling durability, sustaining 65,000 cycles with a minimal capacity decay rate of 0.0004% per cycle. Moreover, a practical Zn||I_2 pouch battery achieves a high capacity of 11.5 mAh and maintains 90.0% capacity retention after 130 cycles. Multiscale spectroscopic characterization and theoretical modeling have collectively elucidated the fundamental mechanisms underlying solvation sheath reorganization and interfacial stabilization. Consequently, this study establishes a scalable molecular engineering pathway for high-performance Zn anodes.

Acknowledgements

This work was supported by the Science and Technology Research and Development Joint Foundation of Henan Province under Project 242301420003 and the National Natural Science Foundation of China under Project 22309164.

Declaration of conflicting interests

The authors declare no conflicting interests regarding the content of this article.

ISSN 2791-0091 (print); 2790-8119 (online)
https://doi.org/10.26599/NRE.2026.9120257
Research Article

Data availability

All data needed to support the conclusions in the paper are presented in the manuscript and/or the Supplementary Materials. Additional data related to this paper may be requested from the corresponding author upon request.

Author contributions

X.L.L. and H.B.D. conceived and designed the experiments. H.W.W. directed the research. W.Y.X., B.F.W., Z.L.C., J.L.L., and Y.C.F. conducted the electrochemical and spectroscopic characterization and data analysis. H.W.W. drafted the manuscript. X.L.L., T.H.X., and H.B.D. provided critical revisions to the manuscript. All authors reviewed, edited, and approved the final version.

Electronic Supplementary Material

Supplementary material (including preparation of electrolytes, assembly of batteries, characterizations, and electrochemical measurements, etc.) is available in the online version of this article at https://doi.org/10.26599/NRE.2026.9120257.

References

[1] Liang, Y. L.; Yao, Y. Designing modern aqueous batteries. *Nat*. *Rev*. *Mater*. **2022**, *8*, 109–122.

[2] Chao, D. L.; Zhou, W. H.; Xie, F. X.; Ye, C.; Li, H.; Jaroniec, M.; Qiao, S. Z. Roadmap for advanced aqueous batteries: From design of materials to applications. *Sci*. *Adv*. **2020**, *6*, eaba4098.

[3] Zhong, C.; Liu, B.; Ding, J.; Liu, X. R.; Zhong, Y. W.; Li, Y.; Sun, C. B.; Han, X. P.; Deng, Y. D.; Zhao, N. Q. et al. Decoupling electrolytes towards stable and high-energy rechargeable aqueous zinc-manganese dioxide batteries. *Nat*. *Energy* **2020**, *5*, 440–449.

[4] Zheng, J. X.; Zhao, Q.; Tang, T.; Yin, J. F.; Quilty, C. D.; Renderos, G. D.; Liu, X. T.; Deng, Y.; Wang, L.; Bock, D. C. et al. Reversible epitaxial electrodeposition of metals in battery anodes. *Science* **2019**, *366*, 645–648.

[5] Yu, X. Y.; Li, Z. G.; Wu, X. H.; Zhang, H. T.; Zhao, Q. A.; Liang, H. F.; Wang, H. A.; Chao, D. L.; Wang, F.; Qiao, Y. et al. Ten concerns of Zn metal anode for rechargeable aqueous zinc batteries. *Joule* **2023**, *7*, 1145–1175.

[6] Sun, W.; Wang, F.; Zhang, B.; Zhang, M. Y.; Küpers, V.; Ji, X.; Theile, C.; Bieker, P.; Xu, K.; Wang, C. S. et al. A rechargeable zinc-air battery based on zinc peroxide chemistry. *Science* **2021**, *371*, 46–51.

[7] Zhou, C. C.; Shan, L. T.; Xing, Z. Y.; Zhou, Y.; Chen, W.; Liang, X. X.; Li, J.; Rao, P.; Kang, Z. Y.; Shi, X. D. et al. Interface layer engineering of zinc anode for durable seawater-based zinc-ion batteries. *Adv*. *Mater*. **2026**, *38*, e16045.

[8] Hong, S. F.; Fang, M. J.; Baffour, S.; Gao, Z. A.; Jin, S.; Xu, H. B.; Yang, R.; Archer, L. A. Highly textured metal anodes for stable aqueous batteries: Fabrication and characterization. *Sci*. *Adv*. **2025**, *11*, eadx0289.

[9] Han, D. L.; Cui, C. J.; Zhang, K. Y.; Wang, Z. X.; Gao, J. C.; Guo, Y.; Zhang, Z. C.; Wu, S. C.; Yin, L. C.; Weng, Z. et al. A non-flammable hydrous organic electrolyte for sustainable zinc batteries. *Nat*. *Sustain*. **2022**, *5*, 205–213.

ISSN 2791-0091 (print); 2790-8119 (online)
https://doi.org/10.26599/NRE.2026.9120257
Research Article
[10] Tang, B. Y.; Shan, L. T.; Liang, S. Q.; Zhou, J. Issues and opportunities facing aqueous zinc-ion batteries. *Energy Environ*. *Sci*. **2019**, *12*, 3288–3304.
[11] Holoubek, J.; Zhang, P.; Serrao, C.; Ai, H. Y.; Choi, I. R.; Greenburg, L. C.; Guan, X.; Cai, A.; Zhang, W. B.; Cui, Y. A solvation-driven reevaluation of organic electrolytes for zinc batteries. *Energy Environ*. *Sci*. **2025**, *18*, 8608–8617.
[12] Wang, M. M.; Ma, J. L.; Meng, Y. H.; Tong, P. Y.; Luo, R. H.; Shen, D. Y.; Zheng, X. H.; Chen, N.; Zhang, M. Y.; Song, L. et al. *In situ* formation of solid electrolyte interphase facilitates anode-free aqueous zinc battery. *eScience* **2025**, *5*, 100397.
[13] Ge, H. Y.; Feng, X. L.; Liu, D. P.; Zhang, Y. Recent advances and perspectives for Zn-based batteries: Zn anode and electrolyte. *Nano Res*. *Energy* **2023**, *2*, e9120039.
[14] Cao, L. S.; Li, D.; Pollard, T.; Deng, T.; Zhang, B.; Yang, C. Y.; Chen, L.; Vatamanu, J.; Hu, E. Y.; Hourwitz, M. J. et al. Fluorinated interphase enables reversible aqueous zinc battery chemistries. *Nat*. *Nanotechnol*. **2021**, *16*, 902–910.
[15] Zhang, L.; Xiao, J.; Xiao, X. L.; Xin, W. L.; Geng, Y. H.; Yan, Z. C.; Zhu, Z. Q. Molecular engineering of self-assembled monolayers for highly utilized Zn anodes. *eScience* **2024**, *4*, 100205.
[16] Zhang, X. M.; Tang, Q.; Luo, H.; Xu, Y. L.; Miao, S. C.; Zhou, S. Y.; Xu, C. H. Y.; Jia, Y.; He, Q. J.; Peng, J. N. et al. Hydrogen bond reconstruction maneuver in eutectic electrolyte enables ultralong-lifespan zinc-ion batteries. *J*. *Am*. *Chem*. *Soc*. **2025**, *147*, 39440–39451.
[17] Dong, D. J.; Wang, T. R.; Sun, Y.; Fan, J.; Lu, Y. C. Hydrotropic solubilization of zinc acetates for sustainable aqueous battery electrolytes. *Nat*. *Sustain*. **2023**, *6*, 1474–1484.
[18] Chen, Y. M.; Zhang, K. J.; Xu, Z. X.; Gong, F. C.; Feng, R. F.; Jin, Z. H.; Wang, X. L. Regulating interfacial reactions through electrolyte chemistry enables an anion-rich interphase for wide-temperature zinc metal batteries. *Energy Environ*. *Sci*. **2025**, *18*, 713–727.
[19] Wang, S. H.; Liu, G. X.; Wan, W.; Li, X. Y.; Li, J.; Wang, C. Acetamide-caprolactam deep eutectic solvent-based electrolyte for stable Zn-metal batteries. *Adv*. *Mater*. **2024**, *36*, 2306546.
[20] Sun, P.; Ma, L.; Zhou, W. H.; Qiu, M. J.; Wang, Z. L.; Chao, D. L.; Mai, W. J. Simultaneous regulation on solvation shell and electrode interface for dendrite-free Zn ion batteries achieved by a low-cost glucose additive. *Angew*. *Chem*., *Int*. *Ed*. **2021**, *60*, 18247–18255.
[21] He, Y. B.; Zhang, R.; Zou, P. C.; Chu, R. W.; Lin, R. Q.; Xu, K.; Xin, H. L. Polyelectrolyte membrane enables highly reversible zinc battery chemistry via immobilizing anion and stabilizing water. *J*. *Am*. *Chem*. *Soc*. **2025**, *147*, 6427–6438.
22] Khan, Z.; Kumar, D.; Crispin, X. Does water-in-salt electrolyte subdue issues of Zn batteries? *Adv*. *Mater*. **2023**, *35*, 2300369.
[23] Shen, Y. F.; Fu, P. J.; Liu, J. J.; Sun, K. S.; Wen, H. Z.; Liu, P.; Lv, H.; Gu, T. T.; Yang, X. D.; Chen, L. Highly stable Zn anodes realized by 3D zincophilic and hydrophobic interphase buffer layer. *Nano Res*. *Energy* **2024**, *3*, e9120115.
[24] Zhang, X. M.; Tang, Q.; Luo, H.; Xie, W. H.; Wang, B. Y.; Zhou, S. Y.; Cao, S. X.; Wang, L. M.; He, Q. J.; Peng, J. N. et al. Multivariate competitive coordination

ISSN 2791-0091 (print); 2790-8119 (online)
https://doi.org/10.26599/NRE.2026.9120257
Research Article
structure in hydrated eutectic electrolytes for ultra-long low-temperature aqueous zinc-ion electrochemistry. *Adv*. *Energy Mater*. **2026**, *16*, e04638.
[25] Chen, Y. Y.; Yin, B. W.; Zeng, Y. X.; Wang, H. F.; Xie, B. B.; Luan, D. Y.; Hu, Y.; Lou, X. W. Ion-dipole-interaction-manipulated bilateral interface chemistry for deep rechargeability and high redox activity of Zn-organic batteries. *Chem* **2025**, *11*, 102411.
[26] Xu, C.; Wang, H. J.; Lei, C. J.; Li, J. Y.; Ma, W. J.; Liang, X. Fast single metal cation conduction in ion-water aggregated aqueous battery electrolytes. *Nat*. *Commun*. **2025**, *16*, 4574.
[27] Zhang, Z. C. Y.; Wang, P.; Wei, C. L.; Feng, J. K.; Xiong, S. L.; Xi, B. J. Synchronous regulation of D-band centers in Zn substrates and weakening Pauli repulsion of Zn ions using the ascorbic acid additive for reversible zinc anodes. *Angew*. *Chem*. **2024**, *136*, e202402069.
[28] Xiao, X. M.; Ye, X. M.; Wu, Z. J.; Wu, X.; Yu, J. Z.; Gu, L.; Liu, S. Trace small molecular/nano-colloidal multiscale electrolyte additives enable ultra-long lifespan of zinc metal anodes. *Adv*. *Mater*. **2024**, *36*, 2408706.
[29] Wang, D. D.; Li, R.; Dong, J. J.; Bai, Z. C.; Wang, N. N.; Dou, S. X.; Yang, J. Bidentate coordination enables anions-regulated solvation structure for advanced aqueous zinc metal batteries. *Angew*. *Chem*., *Int*. *Ed*. **2025**, *64*, e202414117.
[30] Schriber, J. B.; Wallace, A. M.; Cheney, D. L.; Sherrill, C. D. Levels of symmetry-adapted perturbation theory (SAPT). II. Convergence of interaction energy components. *J*. *Chem*. *Phys*. **2025**, *163*, 084114.
[31] Zheng, L. L.; Li, H. H.; Wang, X.; Chen, Z.; Hu, C.; Wang, K. D.; Guo, G. L.; Passerini, S.; Zhang, H. Competitive solvation-induced interphases enable highly reversible Zn anodes. *ACS Energy Lett*. **2023**, *8*, 2086–2096.
[32] Wang, S. X.; Wang, S. N.; Wei, Z. Q.; Wang, Y. Q.; Zhang, D. C.; Chen, Z.; Zhi, C. Y. A parts-per-million scale electrolyte additive for durable aqueous zinc batteries. *Nat*. *Commun*. **2025**, *16*, 1800.
[33] Lin, J. D.; Ji, C. C.; Guo, G. Z.; Luo, Y. L.; Huang, P. R.; Xu, F.; Sun, L. X.; Pfleging, W.; Novoselov, K. S. Interfacial H-bond network/concentration fields/electric fields regulation achieved by D-valine anions realizes the highly efficient aqueous zinc ion batteries. *Angew*. *Chem*. **2025**, *137*, e202501721.
[34] Xu, D. M.; Ren, X. T.; Li, H. Y.; Zhou, Y. R.; Chai, S. M.; Chen, Y. N.; Li, H.; Bai, L. S.; Chang, Z.; Pan, A. Q. et al. Chelating additive regulating Zn-ion solvation chemistry for highly efficient aqueous zinc-metal battery. *Angew*. *Chem*., *Int*. *Ed*. **2024**, *63*, e202402833.
[35] Liu, C.; Li, Q.; Lin, Y. L.; Wei, Z. Q.; Yang, Y. H.; Han, C. P.; Zhu, M. S.; Zhang, H. Y.; Li, H. F. Functional group differentiation of isomeric solvents enables distinct zinc anode chemistry. *Nano Res*. *Energy* **2023**, *2*, e9120064.
[36] Wu, D. R.; Housel, L. M.; King, S. T.; Mansley, Z. R.; Sadique, N.; Zhu, Y. M.; Ma, L.; Ehrlich, S. N.; Zhong, H.; Takeuchi, E. S. et al. Simultaneous elucidation of solid and solution manganese environments via multiphase *operando* extended X-ray absorption fine structure spectroscopy in aqueous Zn/MnO_2 batteries. *J*. *Am*. *Chem*. *Soc*. **2022**, *144*, 23405–23420.

ISSN 2791-0091 (print); 2790-8119 (online)
https://doi.org/10.26599/NRE.2026.9120257
Research Article
[37] Han, D. L.; Wang, Z. X.; Lu, H. T.; Li, H.; Cui, C. J.; Zhang, Z. C.; Sun, R.; Geng, C. N.; Liang, Q. H.; Guo, X. X. et al. A self-regulated interface toward highly reversible aqueous zinc batteries. *Adv*. *Energy Mater*. **2022**, *12*, 2102982.
[38] Wang, J. Y.; Yang, H.; Zhong, Y. P.; Feng, J. R.; Cui, Z.; Chen, R. W.; Chen, J.; Zhao, F. J.; Huang, J. J.; He, G. J. A theory-driven moderation strategy for electrolyte design unlocks stable aqueous zinc deposition. *Angew*. *Chem*., *Int*. *Ed*. **2025**, *64*, e202518262.
[39] Li, Z. G.; Wang, Z. J.; Sun, W. X.; Ma, Y.; Guo, W.; Fu, Y. Z. Regulating interface engineering by Helmholtz plane reconstructed achieves highly reversible zinc metal anodes. *Adv*. *Mater*. **2025**, *37*, 2420489.
[40] Xie, B.; Zheng, C. H.; Lang, H. R.; Li, M.; Hu, Q.; Tan, X.; Zheng, Q. J.; Huo, Y.; Zhao, J. X.; Yang, J. L. et al. Ultrastable electrolyte (>3500 hours at high current density) achieved by high-entropy solvation toward practical aqueous zinc metal batteries. *Energy Environ*. *Sci*. **2024**, *17*, 7281–7293.
[41] Chen, S.; Xia, Y. F.; Zeng, R.; Luo, Z.; Wu, X. X.; Hu, X. Z.; Lu, J.; Gazit, E.; Pan, H. G.; Hong, Z. J. et al. Ordered planar plating/stripping enables deep cycling zinc metal batteries. *Sci*. *Adv*. **2024**, *10*, eadn2265.
[42] Lin, D. W.; Shi, D. H.; Zhu, A. Q.; Yang, C. K.; Zhang, T.; Liu, K.; Liu, K. L.; Hong, G.; Zhang, W. J. Self-adaptive hierarchical hosts with switchable repulsive shielding for dendrite-free zinc-ion batteries. *Adv*. *Energy Mater*. **2024**, *14*, 2304535.
[43] Liu, H. Y.; Ye, Q.; Lei, D.; Hou, Z. D.; Hua, W.; Huyan, Y.; Li, N.; Wei, C. G.; Kang, F. Y.; Wang, J. G. Molecular brush: An ion-redistributor to homogenize fast Zn^{2+} flux and deposition for calendar-life Zn batteries. *Energy Environ*. *Sci*. **2023**, *16*, 1610–1619.
[44] Zheng, J. X.; Cao, Z.; Ming, F. W.; Liang, H. F.; Qi, Z. B.; Liu, W. Q.; Xia, C.; Chen, C. X.; Cavallo, L.; Wang, Z. C. et al. Preferred orientation of TiN coatings enables stable zinc anodes. *ACS Energy Lett*. **2022**, *7*, 197–203.
[45] Wei, F. C.; Xu, H. Y.; Zhang, T. T.; Li, W. D.; Huang, L. Y.; Peng, Y. H.; Guo, H. T.; Wang, Y. X.; Guan, S. J.; Fu, J. W. et al. Mesoporous poly(3,4-ethylenedioxythiophene): Poly(styrenesulfonate) as efficient iodine host for high-performance zinc-iodine batteries. *ACS Nano* **2023**, *17*, 20643–20653.
[46] Zhang, S. J.; Hao, J. N.; Li, H.; Zhang, P. F.; Yin, Z. W.; Li, Y. Y.; Zhang, B. K.; Lin, Z.; Qiao, S. Z. Polyiodide confinement by starch enables shuttle-free Zn-iodine batteries. *Adv*. *Mater*. **2022**, *34*, 2201716.
[47] Xue, Y.; Wang, Y. B.; Zhang, Z. R.; Sun, J.; Li, Q.; He, X. X.; Liu, Z. H.; Lei, Z. B. PEDOT nanowires connecting hollow carbon spheres enable long-cycling Zn-iodine batteries. *Adv*. *Funct*. *Mater*. **2026**, *36*, e19538.
[48] Deng, W. J.; Feng, R. F.; Wang, X. L. Superhalide structure and iodide-proof interphase via electrolyte regulation enable ultrastable zinc-iodine batteries. *Energy Environ*. *Sci*. **2024**, *17*, 8643–8657.
[49] Guo, X. T.; Xu, H. Y.; Tang, Y. J.; Yang, Z. B.; Dou, F.; Li, W. T.; Li, Q.; Pang, H. Confining iodine into metal-organic framework derived metal-nitrogen-carbon for long-life aqueous zinc-iodine batteries. *Adv*. *Mater*. **2024**, *36*, 2408317.

ISSN 2791-0091 (print); 2790-8119 (online)
https://doi.org/10.26599/NRE.2026.9120257
Research Article

[50] Ma, L. B.; Zhu, G. Y.; Wang, Z. W.; Zhu, A. C.; Wu, K. L.; Peng, B.; Xu, J.; Wang, D. H.; Jin, Z. Long-lasting zinc-iodine batteries with ultrahigh areal capacity and boosted rate capability enabled by nickel single-atom electrocatalysts. *Nano Lett*. **2023**, *23*, 5272–5280.

ISSN 2791-0091 (print); 2790-8119 (online)
https://doi.org/10.26599/NRE.2026.9120257
Research Article

A

Hongwei Wang is now a PhD candidate in Condensed Matter Physics at Zhengzhou University. He is working on the development of high-specific-energy and long-life aqueous batteries, with a particular emphasis on electrolyte engineering and interfacial chemistry regulation for advanced energy storage systems.

Tinghui Xiao is a Professor at the School of Physics, Zhengzhou University, Director of the Innovation Center at the Zhongyuan Light Laboratory, and a recipient of the National High-Level Young Talent Program. His research focuses on integrated optics, vibrational spectroscopy, and ultrafast imaging.

Hongbo Ding is an Associate Researcher at the School of Physics, Zhengzhou University. His research primarily focuses on electrochemical energy storage and battery technologies, including aqueous zinc batteries, ionic liquid interfacial engineering, and zinc anode modification.

Xinliang Li is a Professor at the School of Physics, Zhengzhou University. His research primarily focuses on solid-state, halogen, and aqueous batteries, as well as wearable energy storage devices.

ISSN 2791-0091 (print); 2790-8119 (online)
https://doi.org/10.26599/NRE.2026.9120257
Research Article

Electronic Supplementary Material

Multidentate coordination chemistry remodeling solvation sheath and interfacial evolution for robust aqueous Zn battery

Hongwei Wang[1], Wenyu Xu[1], Binfen Wang[1], Zelin Chang[1], Jialin Li[1], Yunchong Feng[1], Tinghui Xiao[1,2]*, Hongbo Ding[1]*, Xinliang Li[1]*

[1]School of Physics and Laboratory of Zhongyuan Light, Zhengzhou University, Zhengzhou 450052, China.
[2]Department of Chemistry, School of Science, The University of Tokyo, Tokyo, 113-0033, Japan
Supporting information to https://doi.org/10.26599/NRE.2026.9120257.

Address correspondence to Hongbo Ding, dinghb@zzu.edu.cn; Xinliang Li, lixinliang@zzu.edu.cn; Tinghui Xiao, xiaoth@zzu.edu.cn

Experiments

Preparation of electrolytes

The bare aqueous electrolyte was prepared by dissolving $ZnSO_4$ (AR grade, Aladdin Reagent Co., Ltd.) in deionized water to obtain a 2 M $ZnSO_4$ solution, designated as BZS. 2-hydroxybutanedioic acid (AR grade, Aladdin Reagent Co., Ltd.) was subsequently introduced into the 2 M $ZnSO_4$ solution at controlled concentrations of 0.05 M, 0.1 M, and 0.2 M to prepare HA-modified electrolytes. The corresponding electrolytes are denoted as 0.05 M HZS, 0.1 M HZS, and 0.2 M HZS, respectively.

Preparation of Iodine (I_2) and activated carbon (AC) cathode

I_2 and AC were uniformly mixed at a 2:1 mass ratio and heated at 120 ºC for 12 h. After cooling naturally to room temperature, the composite was further annealed at 50 ºC for 4 h to remove loosely adsorbed I_2. The resulting I_2/AC material was then combined with conductive carbon black and polyvinylidene fluoride (PVDF) in a mass ratio of 8:1:1. N-methyl-2-pyrrolidone (NMP) was introduced to form a homogeneous slurry, which was subsequently doctor-bladed onto carbon cloth current collectors. The coated electrodes were vacuum-dried at 50 ºC for 12 h to obtain mechanically stable I_2 cathodes. The areal I_2 loading was controlled within 0.8-1.0 mg cm^{-2} or 8.0-10.0 mg cm^{-2} to accommodate different battery configurations.

Assembly of batteries

Symmetric and asymmetric batteries were assembled using CR2032 coin-type cases equipped with polypropylene (PP) sealing rings. The standard assembly components included stainless steel spacers (1.0 mm thickness), spring spacers (stainless steel), working electrodes, and glass fiber separators (Whatman GF/D), with a constant pressure of 1.5 kN applied. For Zn||Zn batteries, Zn foil (Ø14 mm, 99.9%, Canrd Technology Co., Ltd.) served as both the anode and cathode. In Zn||Cu or Zn||Ti

ISSN 2791-0091 (print); 2790-8119 (online)
https://doi.org/10.26599/NRE.2026.9120257
Research Article

batteries, one Zn electrode was replaced with Cu foil (20 μm thick) or Ti foil (20 μm thick), respectively. All coin batteries were filled with 100 μL of electrolyte. Zn||I_2 batteries were constructed using I_2/AC cathodes, Zn anodes, and glass fiber separators. Pouch batteries (3 cm × 3 cm) were fabricated with cathodes of 8.5 mg cm^{-2} mass loading. Electrodes and separators were stacked, vacuum-sealed in aluminum-plastic film, and allowed to rest for 3 h before electrochemical testing to ensure complete electrolyte wetting.

Characterizations

Nuclear magnetic resonance (NMR) spectra were acquired on a Bruker Avance NEO 600 MHz spectrometer. To ensure the high precision of the ^1H NMR measurements and eliminate potential external field fluctuations, a coaxial insert tube containing D_2O with 4,4-dimethyl-4-silapentane-1-sulfonic acid was utilized as a strictly calibrated internal standard. Raman spectroscopy was carried out with a Renishaw spectrometer employing a 532 nm excitation laser. Contact angles were measured using an OCA15EC optical contact-angle meter (DataPhysics Instruments). X-ray diffraction (XRD) patterns were obtained on a Bruker D8 Advance diffractometer with Cu Kα radiation (λ = 0.154 nm), scanning 2θ from 5° to 80°. Surface morphologies of the Zn anodes were examined by scanning electron microscopy (SEM, Zeiss Sigma 360). Topographic analysis was performed *via* atomic force microscopy (AFM, Bruker Dimension Icon). X-ray absorption fine structure (XAFS) spectra were collected in transmission mode using a RapidXAFS 1M spectrometer (Anhui Absorption Spectroscopy Instruments Co., Ltd.), equipped with a Si(533) spherical bent crystal analyzer (500 mm radius), operated at 20 kV and 40 mA. For liquid-phase XAFS measurements, the electrolytes were sealed in a specialized liquid cell with a 2 mm path length following a rigorous degassing procedure to eliminate bubble-induced scattering artifacts. For the ex situ XAFS characterization of cycled Zn anodes, the extracted electrodes were carefully rinsed with deionized water, dried under an argon atmosphere, and stored under vacuum. This strict protocol completely prevented ambient air exposure and artificial oxidation, ensuring pristine sample states before data acquisition.

Electrochemical measurements

Electrochemical measurements including cyclic voltammetry (CV), linear sweep voltammetry (LSV), Tafel curves, chronoamperometry (CA), and electrochemical impedance spectroscopy (EIS) were conducted on a CHI760E electrochemical workstation (Chenhua Instruments, Shanghai, China). CV curves for Zn||Cu batteries were acquired at 2 mV s^{-1} across a potential window of -0.2 to 0.4 V (*vs*. Zn^{2+}/Zn). LSV and Tafel curves were performed in a three-electrode configuration at a scan rate of 1 mV s^{-1}, utilizing Zn foil as the working electrode, Pt foil as the counter electrode, and an Ag/AgCl electrode as the reference. CA profiles were recorded at a constant overpotential of 150 mV in Zn||Zn symmetric batteries. EIS spectra for symmetric batteries were acquired over a frequency range of 100 kHz to 0.1 Hz at ambient temperature. Long-term cycling performance of Zn||Zn, Zn||Cu, Zn||Ti, and Zn||I_2

ISSN 2791-0091 (print); 2790-8119 (online)
https://doi.org/10.26599/NRE.2026.9120257
Research Article

batteries was assessed using a LAND battery-testing system at 25 ºC. The voltage window for the Zn||I_2 batteries was fixed between 0.6 and 1.6 V. For the asymmetric Zn||Cu and Zn||Ti batteries, the stripping cutoff voltage was strictly set to 0.5 V.

Molecular dynamics (MD) simulation methods

Molecular dynamics (MD) simulations of aqueous electrolyte solvation structures were performed using the Gromacs package. Force field parameters were derived from the OPLS all-atom force field. Van der Waals and electrostatic interactions were truncated at a cutoff distance of 15 Å, with long-range electrostatics treated by the particle-particle particle-mesh (PPPM) method. All simulations employed standard periodic boundary conditions [1–3]. Each system first underwent energy minimization to reach a stable configuration. Subsequently, NPT ensemble equilibration was conducted at 298.15 K for 5 ns, followed by a 1000 ps production run in the NVT ensemble for data collection. Temperature and pressure were controlled throughout using the Nosé-Hoover thermostat/barostat algorithm [4].

DFT calculations

DFT calculations of absorption energy on the Zn metal surface were accomplished using the Vienna Ab initio simulation package (VASP) [5]. The generalized gradient approximation (GGA) functionals were considered by Perdew-Burke-Ernzerhof, as well as the projector augmented wave method (PAW-PBE), to describe exchange-correlation effects between electrons [6]. A 40.0-Å vacuum layer was introduced in the Z-axis direction to limit interactions between periodic images. The supercells with a four-layer Zn slab were chosen to represent the adsorbed surface for molecules, and the bottom two layers were fixed to maintain the bulk property. The energy cutoff for the plane-wave basis set was 520 eV, and a Gamma k-mesh of 2×2×1 was adopted. In the optimization process, the convergence criterion for the electronic self-consistent field (SCF) and loop was set to 1×10^{-5} eV/atom. In the single energy process, the convergence criterion for the electronic self-consistent field (SCF) and loop was set to 1×10^{-6} eV/atom. The atomic structures were optimized until the residual forces were below 0.02 eV $Å^{-1}$ [7]. For all calculations, the Van der Waals interaction was taken into account at DFT-D4. The isolated adsorbates were optimized in a box size of 1.5×1.5×1.5 nm^3 with a single gamma k-point. The adsorption energy is calculated via:

$$E_{\mathrm{ads}} = E_{\mathrm{Zn+mol}} - E_{\mathrm{Zn}} - E_{\mathrm{mol}} \quad (1)$$

Where the $E_{\mathrm{Zn+mol}}$, the E_{Zn}, and the E_{mol} represent the total energy of adsorbates on the Zn surface, the energy of the Zn surface, and the energy of the isolated adsorbates, respectively.

Binding energies were performed using the DFT package Gaussian16 under the B3LYP exchange-correlation functional with Grimme's DFT-D3(BJ) empirical dispersion correction, and the ma-TZVP basis set was adopted for self-consistent field (SCF) calculations. Generalized gradient approximation (GGA) parameterized by the Perdew-Burke-Ernzerhof (PBE) formula was employed for evaluating the electron exchange correlation energy. The DFT-D3 method of Grimme was used to describe

ISSN 2791-0091 (print); 2790-8119 (online)
https://doi.org/10.26599/NRE.2026.9120257
Research Article

the weak dispersion forces. The ESP was obtained by Dmol3.

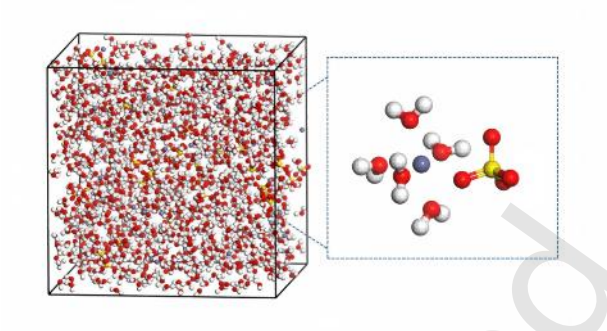

Fig. S1. 3D snapshot from MD simulations of BZS electrolyte. Inset: Magnified view of Zn^{2+} solvation structure within dashed-line box.

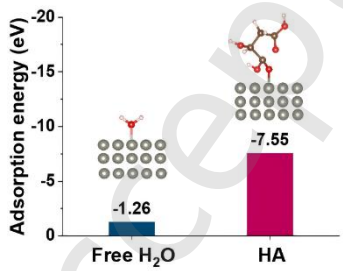

Fig. S2. Adsorption energies of H_2O and HA molecules on Zn anode.

.

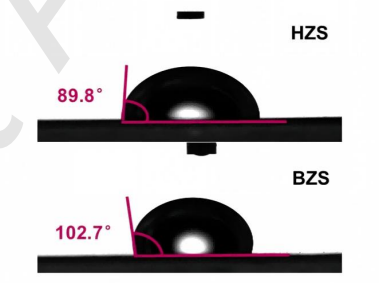

Fig. S3. Contact angles of HZS and BZS electrolyte on Zn anode.

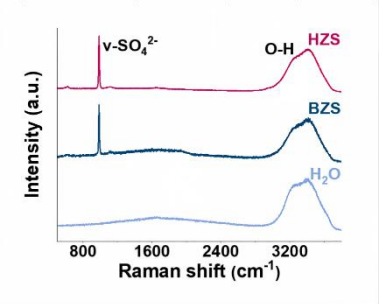

Fig. S4. Raman spectra of HZS electrolyte, BZS electrolyte, and H_2O.

ISSN 2791-0091 (print); 2790-8119 (online)
https://doi.org/10.26599/NRE.2026.9120257
Research Article

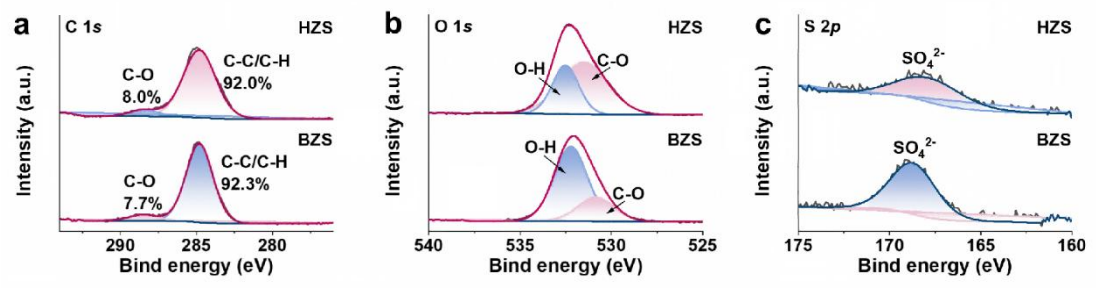

Fig. S5. (**a**) The XPS spectra of C 1*s* on the Zn anodes after 10 cycles. (**b**) The XPS spectra of O 1*s* on the Zn anodes after 10 cycles. (**c**) The XPS spectra of S 2*p* on the Zn anodes after 10 cycles.

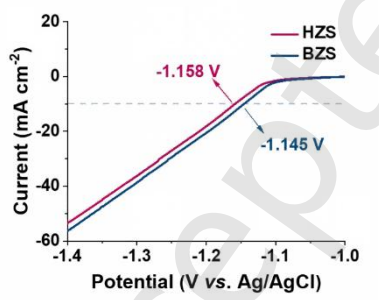

Fig. S6. LSV of HZS and BZS electrolyte.

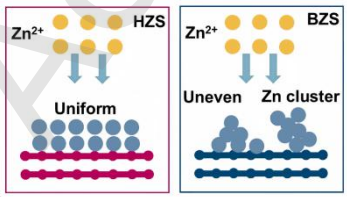

Fig. S7. Schematic illustration of Zn^{2+} deposition mechanisms.

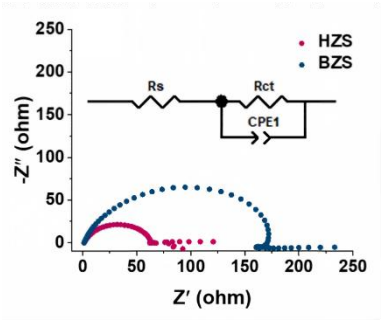

Fig. S8. Nyquist plots of electrochemical impedance spectroscopy for Zn||Zn batteries in HZS and BZS electrolyte.

ISSN 2791-0091 (print); 2790-8119 (online)
https://doi.org/10.26599/NRE.2026.9120257
Research Article

Fig. S9. (**a**) SEM image of Zn anode before cycling. SEM images of cycled Zn anodes (50 cycles, 10 mA cm^{-2}/1 mAh cm^{-2}) in (**b**) HZS electrolyte and (**c**) BZS electrolyte.

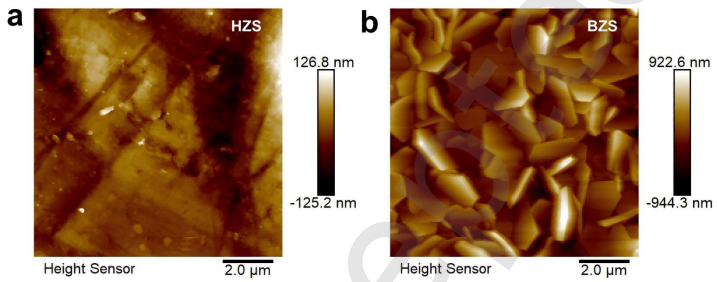

Fig. S10. AFM images of cycled Zn anodes (50 cycles, 10 mA cm^{-2}/1 mAh cm^{-2}) in (**a**) HZS electrolyte and (**b**) BZS electrolyte.

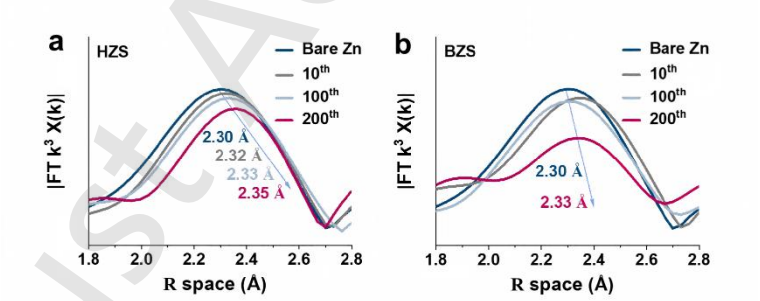

Fig. S11. K^3-weighted FT-EXAFS spectra of bare Zn and cycled anodes (10, 100, 200 cycles) in (**a**) HZS electrolyte and (**b**) BZS electrolyte.

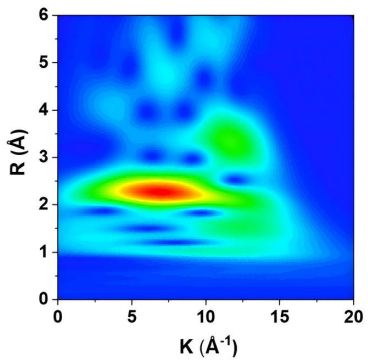

Fig. S12. Wavelet transform (R-space) contour plots of Zn K-edge EXAFS of Zn

ISSN 2791-0091 (print); 2790-8119 (online)
https://doi.org/10.26599/NRE.2026.9120257
Research Article

anode before cycle.

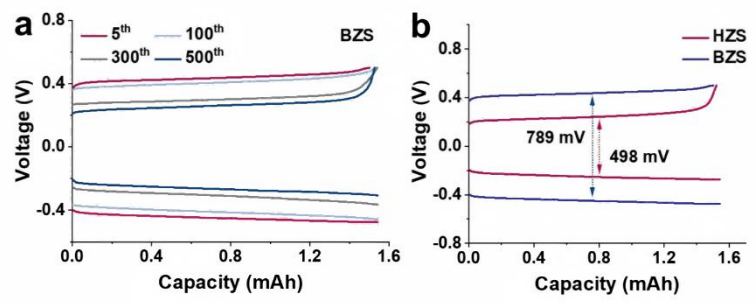

Fig. S13. (**a**) Galvanostatic charge/discharge profiles of Zn||Cu batteries at 20 mA cm^{-2}/1 mAh cm^{-2} across progressive cycles. (**b**) The voltage profiles of Zn||Cu batteries with HZS and BZS electrolyte.

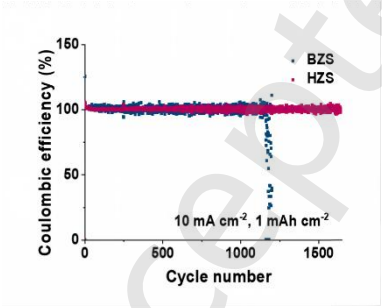

Fig. S14. Coulombic efficiency evolution for Zn||Ti batteries at 10 mA cm^{-2}/1 mAh cm^{-2} in BZS and HZS electrolyte.

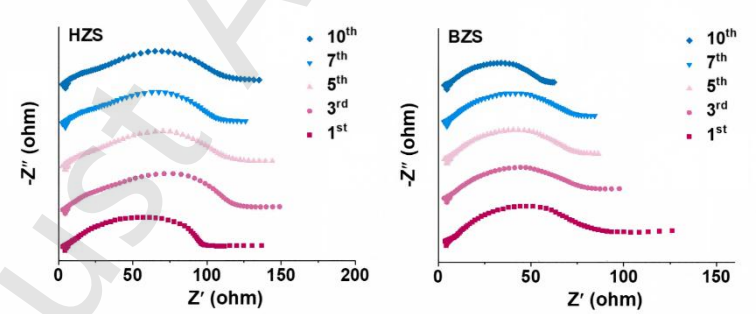

Fig. S15. *In situ* EIS of Zn||Zn batteries with HZS and BZS electrolyte at 1 mA cm^{-2} and 1 mAh cm^{-2} over 10 cycles.

ISSN 2791-0091 (print); 2790-8119 (online)
https://doi.org/10.26599/NRE.2026.9120257
Research Article

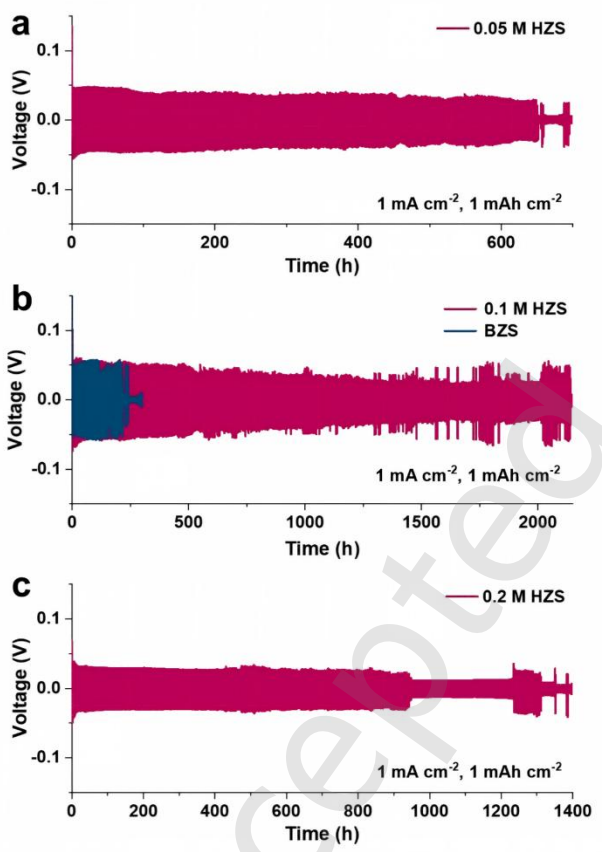

Fig. S16. Cycling performance of Zn||Zn batteries in HZS electrolyte versus (**a**) 0.05 M HZS, (**b**) 0.1 M HZS, and (**c**) 0.2 M HZS electrolytes at 1 mA cm^{-2}/1 mAh cm^{-2}.

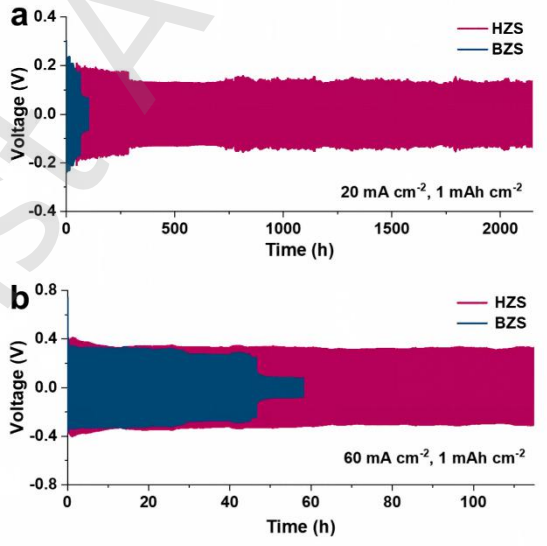

Fig. S17. Cycling performance of Zn||Zn batteries at (**a**) 20 mA cm^{-2}/1 mAh cm^{-2} and (**b**) 60 mA cm^{-2}/1 mAh cm^{-2}.

ISSN 2791-0091 (print); 2790-8119 (online)
https://doi.org/10.26599/NRE.2026.9120257
Research Article

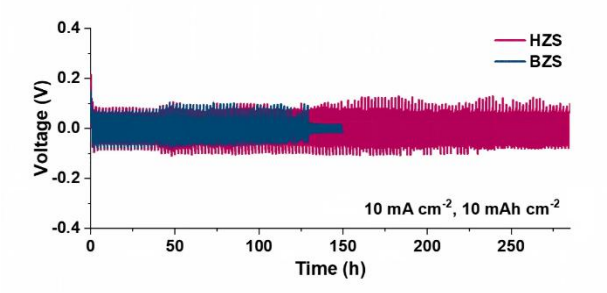

Fig. S18. Cycling performance of Zn||Zn batteries at 10 mA cm^{-2}/10 mAh cm^{-2}.

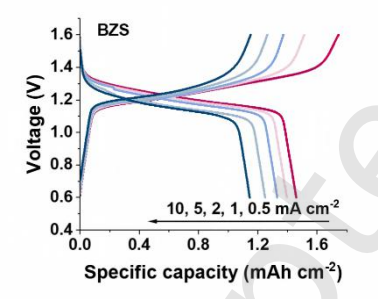

Fig. S19. GCD profiles under various current rates in BZS electrolytes.

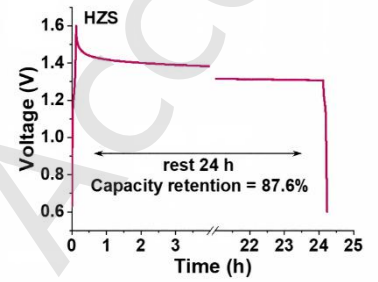

Fig. S20. Self-discharge test curves of Zn||I_2 batteries with HZS electrolyte after resting for 24 h.

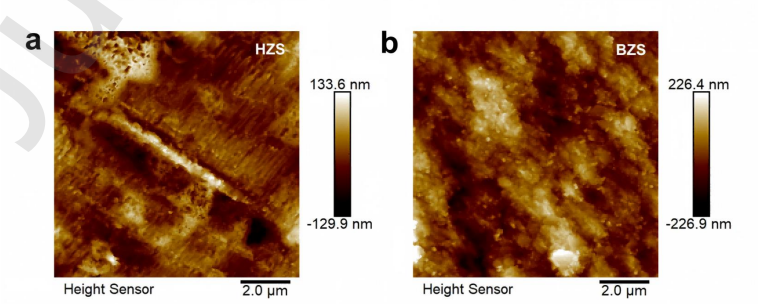

Fig. S21. AFM topography of cycled Zn anodes (500 cycles, 5 A g^{-1}) in HZS and BZS electrolytes.

ISSN 2791-0091 (print); 2790-8119 (online)
https://doi.org/10.26599/NRE.2026.9120257
Research Article

Table S1. Comparison of cumulative capacity, cycle life, and current density with other advanced Zn-based battery systems.

Strategies	Current density ($mA\ cm^{-2}$)	Capacity ($mAh\ cm^{-2}$)	Lifespan (h)	Cumulative capacity ($Ah\ cm^{-2}$)	Ref.
HA	10	1	4600	23.0	This work
	20	1	2150	21.5	
ZAA	20	1	1500	15.0	[8]
NH_4OAc	10	1	1000	5.0	[9]
HDO	1	1	2600	1.3	[10]
PAA	5	1	3292	8.2	[11]
PNO	1	1	2300	1.1	[12]
HESE	5	5	3500	8.7	[13]
NaDFOB	5	1	4100	10.2	[14]
TES-Na	10	1	1700	8.5	[15]
TETA	10	10	2500	12.5	[16]
HSL	2	2	3800	3.8	[17]
SAP-GF	10	5	600	3.0	[18]
SAB-Zn	20	10	1100	11.0	[19]
C-CNT	4	1	3000	6.0	[20]
PSPMA	10	5	2500	12.5	[21]
Bi/Bi_2O_3	1	1	3120	3.1	[22]
DCS	5	1	2000	5.0	[23]
ZP@Zn	20	5	470	4.7	[24]
BTO/Zn	10	2	1300	6.5	[25]
TiN@Zn	1	1	2300	1.1	[26]
ZA	5	1	4268	10.6	[27]
ANF	5	2.5	850	2.1	[28]
HNT-GF	5	1	2000	5.0	[29]
gBC	1	1	2900	1.5	[30]
BC-BTO	5	2.5	1200	3.0	[31]

Table S2. Comparative benchmarking against state-of-the-art $Zn||I_2$ batteries.

Strategies	Current density ($A\ g^{-1}$)	Specific capacity ($mAh\ g^{-1}$)	Cycle number	Ref.
HA	10	150	65000	This work
RABA-H	1	60	5500	[32]
mPEDOT: PSS	5	95	20000	[33]
Starch	10	75	50000	[34]
I_2-P-HCS	10	121	47000	[35]
S-3@I_3^-	5C	108.4	4000	[36]
DCS	10	135	40000	[23]
MEOH-Ti	5	127	45000	[37]

ISSN 2791-0091 (print); 2790-8119 (online)
https://doi.org/10.26599/NRE.2026.9120257
Research Article

EMIM[OAc]	4	149.23	18000	[38]
ZS-2AEC	2	148.4	16000	[39]
M9/I_2	2	161.9	10000	[40]
Pyridine	10	105.5	25000	[41]
mPD@rGO	10	99.2	35000	[42]
I_2/NiSAs	10C	151	10000	[43]
SC-PPS	3.2	84.6	6000	[44]

Table S3. Techno-economic assessment of the BZS and HZS electrolytes.

Electrolyte	Component	Estimated bulk price ($/kg)	Amount per liter electrolyte (g/L)	Cost per liter electrolyte ($/L)
BZS	2 M $ZnSO_4 \cdot 7H_2O$	1.5	575.0	0.86
HZS	2 M $ZnSO_4 \cdot 7H_2O$ 0. 1 M HA	3.5	13.4	0.91

Supplementary note: The estimated bulk prices are derived from contemporary industrial chemical suppliers for ton-scale commercial procurement. The HA additive cost is calculated based on its industrial-grade bulk purchase price. The HZS electrolyte incurs a negligible cost increase of approximately $0.047/L (~5.4%) over the standard BZS electrolyte, demonstrating superior commercial scalability relative to electrolytes that employ expensive fluorinated salts or complex custom additives.

References

1. Willman, J. T.; Nguyen-Cong, K.; Williams, A. S.; Belonoshko, A. B.; Moore, S. G.; Thompson, A. P.; Wood, M. A.; Oleynik, I. I. Machine learning interatomic potential for simulations of carbon at extreme conditions. *Phys. Rev.B* **2022**, 106, L180101.
2. Kaminski, GA.; Friesner, RA.; Tirado-Rives, J.; Jorgensen, WL. Evaluation and reparametrization of the OPLS-AA force field for proteins via comparison with accurate quantum chemical calculations on peptides. *J. Phys. Chem. B* **2001**, 105, 6474-6487.
3. Dodda, LS.; Vilseck, JZ.; Tirado-Rives, J.; Jorgensen, WL. 1.14* CM1A-LBCC: localized bond-charge corrected CM1A charges for condensed-phase simulations. *J. Phys. Chem. B* **2017**, 121, 3864-3870.
4. Jewett, Andrew I.; Stelter, D.; Lambert, J.; Saladi, S. M.; Roscioni, O. M.; Ricci, M.; Autin, L.; Maritan, M.; Bashusqeh, S. M.; Keyes, T. Moltemplate: A tool for coarse-grained modeling of complex biological matter and soft condensed matter physics. *J. Mol. Biol.* **2021**, 433, 166841.
5. Kresse, G.; Furthmüller, J. Efficiency of ab-initio total energy calculations for metals and semiconductors using a plane-wave basis set. *Comp. Mater. Sci.* **1996**, 6, 15-50.

ISSN 2791-0091 (print); 2790-8119 (online)
https://doi.org/10.26599/NRE.2026.9120257
Research Article

6. Blöchl, PE.; Jepsen, O. Andersen, OK. Improved tetrahedron method for Brillouin-zone integrations. *Phys. Rev.B* **1994**, 49, 16223.
7. Caldeweyher, E.; Bannwarth, C.; Grimme, S. Extension of the D3 dispersion coefficient model. *J. Chem. Phys.* **2017**, 147, 034112.
8. Xiao, X. M.; Ye, X. M.; Wu, Z. J.; Wu, X.; Yu, J. Z.; Gu, L.; Liu, S. Trace small molecular/nano-colloidal multiscale electrolyte additives enable ultra-long lifespan of zinc metal anodes. *Adv. Mater.* **2024**, 36, 2408706.
9. Han, D. L.; Wang, Z. X.; Lu, H. T.; Li, H.; Cui, C. J.; Zhang, Z. C.; Sun, R.; Geng, C. N.; Liang, Q. H.; Guo, X. X. *et al.* A self-regulated interface toward highly reversible aqueous zinc batteries. *Adv. Energy Mater.* **2022**, 12, 2102982.
10. Wang, J. Y.; Yang, H.; Zhong, Y. P.; Feng, J. R.; Cui, Z.; Chen, R. W.; Chen, J.; Zhao, F. J.; Huang, J. J.; He, G. J. A theory-driven moderation strategy for electrolyte design unlocks stable aqueous zinc deposition. *Angew. Chem. Int. Edit.* **2025**, 64, e202518262.
11. Ouyang, K. F.; Li, F.; Ma, D. T.; Wang, Y. Y.; Shen, S. C.; Yang, M.; Qiu, J. M.; Wen, W. T.; Zhao, N.; Mi, H. W. *et al.* Trace-additive-mediated hydrophobic structure editing of aqueous zinc metal batteries for enabling all-climate long-term operation. *ACS Energy Lett.* **2023**, 8, 5229-5239.
12. Li, Z. G; Wang, Z. J.; Sun, W. X.; Ma, Y.; Guo, W.; Fu, Y. Z. Regulating interface engineering by Helmholtz plane reconstructed achieves highly reversible zinc metal anodes. *Adv. Mater.* **2025**, 37, 2420489.
13. Xie, B.; Zheng, C. H.; Lang, H. R.; Li, M.; Hu, Q.; Tan, X.; Zheng, Q. J.; Huo, Y.; Zhao, J. X.; Yang, J. L. *et al.* Ultrastable electrolyte (>3500 hours at high current density) achieved by high-entropy solvation toward practical aqueous zinc metal batteries. *Energy Environ. Sci.* **2024**, 17, 7281-7293.
14. Tang, S.; Wei, Q. Y.; Liu, B. Q.; Yang, J. L.; Jiang, H. Z.; Ge, Y. Z.; Wu, D. X.; Li, J.; Qiu, T. Y.; Zhang, H. *et al.* Simultaneous manipulation of electric double layer and Zn (100) deposition enabled by anions for highly stable Zn anodes. *Angew. Chem. Int. Edit.* **2025**, 64, e202510252.
15. Ding, H. L.; Lin, Z. X.; Lin, X. T.; Chen, J. C.; Huang, X. X.; Ye, M. H.; Wen, Z. P.; Tang, Y. C.; Liu, X. Q.; Zhang, Y. F. *et al.* Interrupting the hydroxide enrichment-induced electrode degradation loop for achieving stable aqueous Zn-I_2 batteries. *Angew. Chem. Int. Edit.* **2025**, 64, e202513993.
16. Wang, S. X.; Huang, Z. D.; Zhu, J. X.; Wang, Y. Q.; Li, D. D.; Wei, Z. Q.; Hong, H.; Zhang, D. C.; Xiong, Q.; Li, S. M. *et al.* Quantifying asymmetric zinc deposition: A guide factor for designing durable zinc anodes. *Adv. Mater.* **2024**, 36, 2406451.
17. Yang, T. Y.; Su, T. T.; Xu, M.; Wang, D. D.; Ren, W. F.; Dou, H. Z.; Sun, R. C.; Chen, Z. W. Dienoic-acid coupling effect induced hierarchical interface for high-performance zinc metal batteries. *Angew. Chem. Int. Edit.* **2025**, 64, e202512780.

ISSN 2791-0091 (print); 2790-8119 (online)
https://doi.org/10.26599/NRE.2026.9120257
Research Article

18. Zhang, Y.; Zhang, Y. X.; Deng, J.; Xue, R. R.; Yang, S. C.; Ma, Y.; Wang, Z. H. In situ electrochemically-bonded self-adapting polymeric interface for durable aqueous zinc ion batteries. *Adv. Funct. Mater.* **2024**, 34, 2310995.
19. Chen, S.; Xia, Y. F.; Zeng, R.; Luo, Z.; Wu, X. X.; Hu, X. Z.; Lu, J.; Gazit, E.; Pan, H. G.; Hong, Z. J. *et al.* Ordered planar plating/stripping enables deep cycling zinc metal batteries. *Sci. Adv.* **2024**, 10, eadn2265.
20. Lin, D. W.; Shi, D. H.; Zhu, A. Q.; Yang, C. K.; Zhang, T.; Liu, K.; Liu, K. L.; Hong, G.; Zhang, W. J. Self-Adaptive Hierarchical hosts with switchable repulsive shielding for dendrite-free zinc-ion batteries. *Adv. Energy Mater.* **2024**, 14, 2304535.
21. Liu, H. Y.; Ye, Q.; Lei, D.; Hou, Z. D.; Hua, W.; Huyan, Y.; Li, N.; Wei, C. G.; Kang, F. Y.; Wang, J. G. Molecular brush: an ion-redistributor to homogenize fast Zn^{2+} flux and deposition for calendar-life Zn batteries. *Energy Environ. Sci.* **2023**, 16, 1610-1619.
22. Tian, X. M.; Zhao, Q.; Zhou, M. M.; Huang, X. J.; Sun, Y.; Duan, X. G.; Zhang, L.; Li, H.; Su, D. W.; Jia, B. H. *et al.* Synergy of dendrites-impeded atomic clusters dissociation and side reactions suppressed inert interface protection for ultrastable Zn anode. *Adv. Mater.* **2024**, 36, 2400237.
23. Yao, W. X.; Liu, Z. X.; Wang, M.; Xiao, Z. Q.; Xiao, X.; Zhou, G. M. Surface segregation reconstructing alloy substrate for ultra-stable zinc-based batteries. *Adv. Mater.* **2025**, 38, e10483.
24. Xing, Z. Y.; Sun, Y. Y.; Xie, X. S.; Tang, Y.; Xu, G. F.; Han, J. W.; Lu, B. A.; Liang, S. Q.; Chen, G.; Zhou, J. Zincophilic electrode interphase with appended proton reservoir ability stabilizes Zn metal anodes. *Angew. Chem. Int. Edit.* **2023**, 62, e202215324.
25. Zou, P. C.; Zhang, R.; Yao, L. B.; Qin, J. Y.; Kisslinger, K.; Zhuang, H. L.; Xin, H. L. Ultrahigh-rate and long-life zinc–metal anodes enabled by self-accelerated cation migration. *Adv. Energy Mater.* **2021**, 11, 2100982.
26. Zheng, J. X; Cao, Z.; Ming, F. W.; Liang, H. F.; Qi, Z. B.; Liu, W. Q.; Xia, C.; Chen, C. X.; Cavallo, L. G.; Wang, Z. C. *et al.* Preferred orientation of TiN coatings enables stable zinc anodes. *ACS Energy Lett.* **2022**, 7, 197-203.
27. Zhou, C. C.; Shan, L. T.; Xing, Z. Y.; Zhou, Y.; Chen, W.; Liang, X. X.; Li, J.; Rao, P.; Kang, Z. Y.; Shi, X. D. *et al.* Interface layer engineering of zinc anode for durable seawater-based zinc-ion batteries. *Adv. Mater.* **2025**, 38, e16045.
28. Yang, L.; Zhu, Y. J.; Yu, H. P.; Wang, Z. Y.; Cheng, L.; Li, D. D.; Tao, J. C.; He, G.; Li, H. A Five Micron thick aramid nanofiber separator enables highly reversible Zn anode for energy-dense aqueous zinc-ion batteries. *Adv. Energy Mater.* **2024**, 14, 2401858.
29. Liu, S. W.; Han, Q. Z.; He, C. W.; Xu, Z. J.; Huang, P. F.; Cai, L. C.; Chen, H. Q.; Zheng, H. N.; Zhou, Y. J.; Wang, M. Y. *et al.* Ion-sieving separator functionalized by natural mineral coating toward ultrastable Zn metal anodes. *ACS Nano* **2024**, 18, 25880-25892.
30. Dong, Y. Y.; Fan, W. J.; Wang, X. J.; Huang, H. S.; Zhu, Y.; Chen, J. W.; Tian, W. Q.; Huang, Y. H.; Wu, J. Y. Hydrophobicity gradient in ultrathin cellulose

ISSN 2791-0091 (print); 2790-8119 (online)
https://doi.org/10.26599/NRE.2026.9120257
Research Article

separators for durable seawater-based zinc batteries. *Adv. Funct. Mater.* **2025**, 36, e13685.

31. Tan, Y. C.; Chen, D.; Liu, Y. H.; Zhang, Y. M.; Yao, T. Y.; Miao, C. L.; Yang, H.; Li, L.; Kotsiubynskyi, V.; Li, G. S. *et al.* Modulating electric field by high-permittivity surface medium to enable homogeneous Zn deposition for Zn metal anode. *J. Energy Chem.* **2025**, 110, 246-254.
32. Tan, Y. C.; Chen, D.; Liu, Y. H.; Zhang, Y. M.; Yao, T. Y.; Miao, C. L.; Yang, H.; Li, L.; Kotsiubynskyi, V.; Li, G. S. *et al.* Optimizing interface multi-physical fields via (R)-3-aminobutyric acid cations for enhanced zinc deposition behavior realizes the highly efficient zinc-iodine batteries. *Adv. Energy Mater.* **2025**, 15, e03616.
33. Wei, F. C.; Xu, H. Y.; Zhang, T. T.; Li, W. D.; Huang, L. Y.; Peng, Y. H.; Guo, H. T.; Wang, Y. X.; Guan, S. J.; Fu, J. W. *et al.* Mesoporous poly(3,4-ethylenedioxythiophene): Poly(styrenesulfonate) as efficient iodine host for high-performance zinc-iodine batteries. *ACS Nano* **2023**, 17, 20643-20653.
34. Zhang, S. J.; Hao, J. N.; Li, H.; Zhang, P. F.; Yin, Z. W.; Li, Y. Y.; Zhang, B. K.; Lin, Z.; Qiao, S. Z. Polyiodide confinement by starch enables shuttle-free Zn–iodine batteries. *Adv. Mater.* **2022**, 34, 2201716.
35. Xue, Y.; Wang, Y. B.; Zhang, Z. R.; Sun, J.; Li, Q.; He, X. X; Liu, Z. H.; Lei, Z. B. PEDOT nanowires connecting hollow carbon spheres enable long-cycling Zn-iodine batteries. *Adv. Funct. Mater.* **2025**, 36, e19538.
36. Zhang, L. Q.; Luo, K.; Gong, J. M.; Zhou, Y. Z.; Guo, H. L.; Yu, Y.; He, G. J.; Gohy, J. F..; Parkin, I. P.; Hofkens, J. *et al.* Unlocking durable and sustainable zinc–iodine batteries via molecularly engineered polyiodide reservoirs. *Angew. Chem. Int. Edit.* **2025**, 64, e202506822.
37. Deng, W. J.; Feng, R. F.; Wang, X. L. Superhalide structure and iodide-proof interphase via electrolyte regulation enable ultrastable zinc-iodine batteries. *Energy Environ. Sci.* **2024**, 17, 8643-8657.
38. Xiao, T.; Yang, J. L.; Zhang, B.; Wu, J. W.; Li, J. L.; Mai, W. J.; Fan, H. J. All-round ionic liquids for shuttle-free zinc-iodine battery. *Angew. Chem. Int. Edit.* **2024**, 63, e202318470.
39. Li, W.; Chen, M. F.; Zhou, Q. Q.; Mi, X. X.; Zhao, H. R.; Liu, B.; Chen, J. Z.; Yao, Y. G. Combining inner Helmholtz plane adjustment and Gibbs–Thomson effect to enable ultra-high utilization of zinc electrodes and inhibit polyiodide shuttling. *Adv. Funct. Mater.* **2025**, 36, e13773.
40. Guo, X. T.; Xu, H. Y.; Tang, Y. J.; Yang, Z. B.; Dou, F.; Li, W. T.; Li, Q.; Pang, H. Confining iodine into metal-organic framework derived metal-nitrogen-carbon for long-life aqueous zinc-iodine batteries. *Adv. Mater.* **2024,** 36, 2408317.
41. Lyu, Y. Q.; Yuwono, J. A.; Wang, P. T.; Wang, Y. Y.; Yang, F. H.; Liu, S. L.; Zhang, S. L.; Wang, B. F.; Davey, K.; Mao, J. F. *et al.* Organic pH buffer for dendrite‐free and shuttle‐free Zn‐I_2 batteries. *Angew. Chem. Int. Edit.* **2023**, 62, e202303011.

ISSN 2791-0091 (print); 2790-8119 (online)
https://doi.org/10.26599/NRE.2026.9120257
Research Article

42. Wei, F. C.; Zhang, T. T.; Xu, H. Y.; Peng, Y. H.; Guo, H. T.; Wang, Y. X.; Guan, S. J.; Fu, J. W.; Jing, C. B.; Cheng, J. G. *et al.* 2D Mesoporous naphthalene-based conductive heteroarchitectures toward long-life, high-capacity zinc-iodine batteries. *Adv. Funct. Mater.* **2024**, 34, 2310693.
43. Ma, L. B.; Zhu, G. Y.; Wang, Z. W.; Zhu, A. C.; Wu, K. L.; Peng, B.; Xu, J.; Wang, D. H.; Jin, Z. Long-lasting zinc–iodine batteries with ultrahigh areal capacity and boosted rate capability enabled by nickel single-atom electrocatalysts. *Nano Letters* **2023**, 23, 5272-5280.
44. Zhang, L. Q.; Huang, J. J.; Guo, H. L.; Ge, L. F.; Tian, Z. H.; Zhang, M. J.; Wang, J. T.; He, G. J.; Liu, T. X.; Hofkens, J. Tuning ion transport at the anode‐electrolyte interface via a sulfonate‐rich ion‐exchange layer for durable zinc‐iodine batteries. *Adv. Energy Mater.* **2023**, 13, 2203790.